AGU100 ADVANCING EARTH AND SPACE SCIENCE

JGR

Journal of Geophysical Research: Atmospheres

RESEARCH ARTICLE

10.1029/2017JD028150

Special Section:
Water-soil-air-plant-human nexus: Modeling and observing complex land-surface systems at river basin scale

Key Points:
- Anomalous glacier state in the catchments of Muzart and Karayulgun rivers, Central Tianshan, was revealed by geodetic measurements
- Systematic biases in the height difference maps are subtly tuned and compensated to improve measurement accuracy
- Strong capability of cold storage and temperature drop may be the main reasons for the anomalous mass changes

Correspondence to:
J. Li,
lijia20050710@csu.edu.cn

Citation:
Li, Z., Li, J., Ding, X., Wu, L., Ke, L., Hu, J., et al. (2018). Anomalous glacier changes in the southeast of Tuomuer-Khan Tengri Mountain Ranges, Central Tianshan. *Journal of Geophysical Research: Atmospheres*, *123*, 6840–6863. https://doi.org/10.1029/2017JD028150

Received 2 DEC 2017
Accepted 12 JUN 2018
Accepted article online 20 JUN 2018
Published online 11 JUL 2018

Anomalous Glacier Changes in the Southeast of Tuomuer-Khan Tengri Mountain Ranges, Central Tianshan

Zhi-wei Li[1], Jia Li[1,2], Xiao-li Ding[2], Li-xin Wu[1], Ling-hong Ke[2], Jun Hu[1], Bing Xu[1], and Fen Peng[2]

[1]School of Geosciences and Info-Physics, Central South University, Changsha, Hunan, China, [2]Department of Land Surveying and Geo-Informatics, Hong Kong Polytechnic University, Kowloon, Hong Kong

Abstract Central Tianshan (CTS) plays a prominent role in maintaining the vulnerable ecosystem in Central Asia. Rivers originating from it have high proportions of the runoffs contributed by glacier meltwater. In this study, the glacier mass balance in the catchments of Muzart and Karayulun rivers, CTS, was estimated by a geodetic method based on Advanced Land Observing Satellite/Panchromatic Remote-sensing Instrument for Stereo Mapping images and Shuttle Radar Topography Mission (SRTM) digital elevation model (DEM). The results revealed that at the west and east glacial centers in the study area, the 2000–2011 mass loss rates were −0.03 ± 0.17 and −0.06 ± 0.17 m w.e./a, respectively, considerably lower than other CTS zones. In order to ascertain this stable glacier state, we also performed a geodetic measurement based on TerraSAR-X add-on for Digital Elevation Measurement (TanDEM-X) images and SRTM DEM (2000–2012), and the results are similar (0.01 ± 0.17 and −0.04 ± 0.17 m w.e./a, respectively). The glacier thickness change around the regional snowline was close to zero. The strong capability of cold storage and the temperature drop in the early 21st century may account for the anomalous mass changes. Despite slight overall mass changes, obvious thinning was observed on many exposed glacier feet. This study indicates that the glacier melting can be effectively controlled if the rising trend of temperatures is reversed; furthermore, the land surface hydrological model should be calibrated with geodetic glacier mass balance measurement when it is used to simulate the streamflow trend in the headwater basin.

1. Introduction

In many remote inland regions, mountain glaciers serve as vital freshwater resources for the ecosystem and domestic agricultural and industrial activities (Li et al., 2008; Sorg et al., 2012). Lives and glaciers are connected by the rivers originating from the high-mountains glacier melting. At present, the inland growing population and domestic economic development have generated mounting pressure on freshwater supplies (Peduzzi et al., 2010). However, the glacier meltwater flow is becoming increasingly unstable because of climate warming. Dramatic glacier shrinkage causes runoff increase that may lead to floods/mudflow. When most glacier mass loses, droughts will occur in the basin where most population concentrates. Hence, there is an urgent need to investigate the mass balance of glaciers within river catchments, to support the planning of agricultural and industrial production and the formation of a proper hydrological policy (Schiefer et al., 2007).

Glacier spatial extent and ice thickness changes are the essential parameters for determining mass balance. Due to the publicly available medium-resolution optical images and relatively simple procedure, the measurement of glacier spatial extent fluctuation has been conducted much more widely than that of ice thickness change. Both glacier terminus retreat and frontier shrinkage (usually occurring in the glacier tongue) can be deemed as indicators of a negative mass balance, and vice versa. However, care must be taken when drawing such conclusions (Bamber & Rivera, 2007; Gardelle et al., 2013; Vincent et al., 2013; Zhou et al., 2017), because the area changes in the lower parts of glaciers cannot reflect the mass changes in the upper reaches, and quantitative mass changes cannot be determined when the ice thickness changes are not available. Furthermore, for the glaciers whose tongues are covered by thick debris, mass loss basically takes the form of down-wasting (stationary thinning) rather than retreat or shrinkage (Bolch et al., 2011; Scherler et al., 2011), and for surge-type glaciers, a rapid advance can enlarge the ice-covered area without affecting or even reducing overall mass. Hence, an unambiguous and quantitative estimate of mass balance should be based on ice thickness changes.

Although in-site glaciological measurement is a highly accurate way of estimating glacier thickness changes, it is labor-intensive and its spatial coverage is limited (Racoviteanu et al., 2007). In comparison, geodetic measurement, that is, deriving a new digital elevation model (DEM) and subtracting it from a historical one, can obtain both spatially and temporally comprehensive thickness changes at a relatively low cost. Therefore, geodetic measurement is deemed as one of the most practical approaches for achieving a statistically representative sample of mass balance estimates at regional scale (Bamber & Rivera, 2007). Photogrammetry is an effective technique for generating a DEM. However, the accuracy of photogrammetry is significantly impacted by the distribution and accuracy of the ground control points (GCPs). Ideally, GCPs need to be evenly distributed throughout the image and have decimeter-level accuracy. Since mountain glaciers generally locate in remote and hostile environments, the collection of field GCPs is very difficult. If a precise historical topographic map is not available, the absence of GCPs will severely limit the accuracy of the photogrammetry. Other measurements such as space-borne laser altimetry products are also highly accurate (decimeter-level accuracy) but offer very poor spatial coverage on glaciers in midlatitude mountain areas. Therefore, laser altimetry measurements must be extrapolated to provide an estimate of the thickness change for a whole glacial region, which may produce significantly biased results. The Ice, Cloud, and Land Elevation Satellite/Geoscience Laser Altimeter System (ICESat/GLAS) GLA14 product, which is a space-borne laser altimetry land elevation product, has been released for scientific research purposes. We thus have the chance to adopt the ICESat/GLAS elevation data as the GCPs for photogrammetry (Atwood et al., 2007; Nuth & Kääb, 2011). This along with the orthorectified U.S. Geological Survey (USGS) Landsat-7/ETM+ L1T images offers us the opportunity to generate sufficiently accurate DEMs over glacial regions, without use of field GCPs (Pieczonka et al., 2013). In such a way, the advantages of laser altimetry and photogrammetry are inherited. More precisely, the laser altimetry ensures the accuracy, and the photogrammetry guarantees the extensive spatial coverage of the measurements.

Known as the "Water Tower of Central Asia," Tianshan is one of the most notable geographic names in cryosphere family. Because of the vast spatial extent, scholars divide it into five parts, that is, Eastern, Northern, Central, Inner, and Western Tianshan. In terms of glaciation, Central Tianshan (CTS) is the core area. Its glacier area occupies about 56.6% of that of the entire Tianshan (Li et al., 2017). Although glacier mass change studies associated with CTS has evidently increased in recent years, there is still plenty of fine-scale glacier change knowledge that are unknown and worthy of exploring, because the local topography and climate patterns vary from mountain to mountain. In the catchments of Muzart and Karayulun rivers, southeast of the Tuomuer Khan-Tengri Mountain Ranges (major part of the CTS; see Figure 1), an Advanced Land Observing Satellite/Panchromatic Remote-sensing Instrument for Stereo Mapping (ALOS/PRISM) stereo image, with fine resolution and high base-to-height ratio, was acquired on 29 August 2010. Previously, Lamsal et al. (2011), Shangguan et al. (2015), Holzer et al. (2015), and Ye et al. (2015) adopted ALOS/PRISM stereo images of 2006, 2007, 2009, and 2006 to study the elevation changes of the Imja glacier (Himalaya), the Southern Inylchek glacier (CTS), the Muzagh Ata glacial center (eastern Pamir), and the Rongbuk Catchment glacial center (northern slope of Mt. Everest), respectively. The usefulness of the ALOS/PRISM stereo image on high-mountain glacier studies has been proven. However, the stereo model computation in the above four studies relied on GCPs obtained by in-site measurements or extracted from topographic maps or the Shuttle Radar Topography Mission (SRTM) DEM. The numbers of effective GCPs are generally scarce, or their quality are not ensured (e.g., those extracted from SRTM DEM), which degrade the quality of the mass balance measurements.

In this study, we adopt the geodetic method based on photogrammetry to investigate the early 21st century glacier mass changes in the catchments of Muzart and Karayulun rivers, CTS. The ALOS/PRISM stereo images, the ICESat/GLAS GLA14 product, the Landsat-7/ETM+ L1T images, and the SRTM DEM are selected as stereo imagery, height control source, horizontal control source, and historical DEM, respectively, for generating a new DEM. Whether it is individual (Fujita et al., 2011; Kronenberg et al., 2016; Shangguan et al., 2015; WGMS, 2015), subregional (Petrakov et al., 2016; Pieczonka et al., 2013), or region scale (Li et al., 2017), quantitative glacier mass changes measurements have suggested that the glaciers in CTS are not exceptional under the background of global warming (see Table 1). Most of them were found to experience considerable decline in the early 21st century. However, this study found a nearly stable glacierized zone spreading over 150 km^2 in the CTS. In order to confirm this "anomalous" result, we also performed a geodetic glacier mass balance measurement based on InSAR and analyzed the results from the aspect of glacier motion fields and with the aid of meteorological data. Although the Tuomuer-Khan Tengri Mountain Ranges where the catchments of the Muzart and Karayulun rivers are located in its southeast is a huge glacial center, the

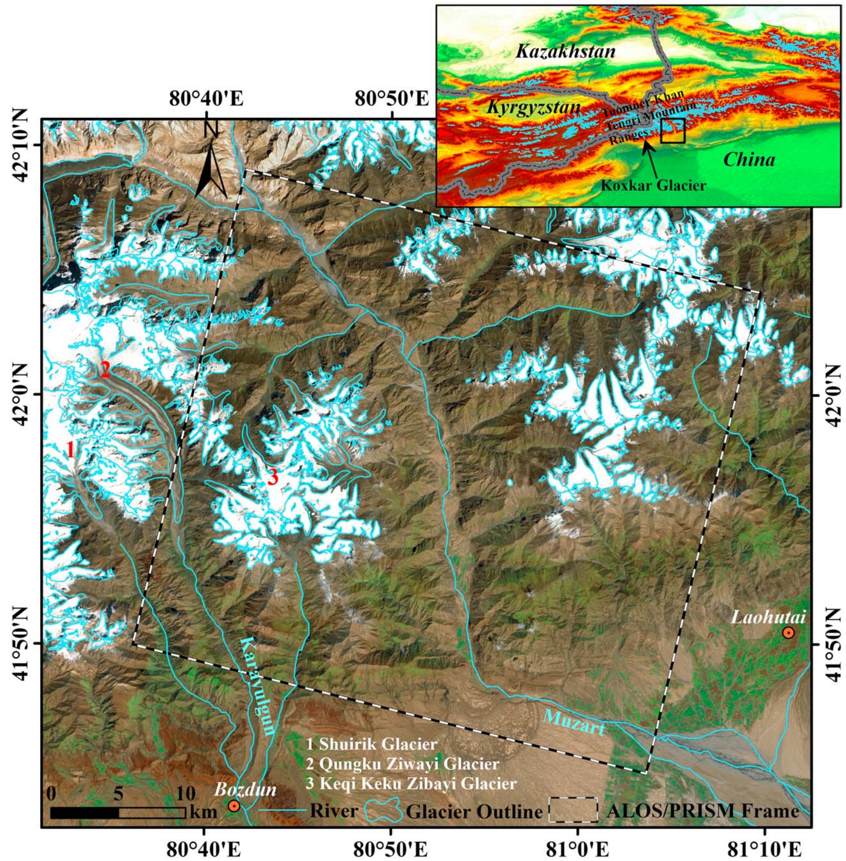

Figure 1. The study area shown in the Landsat image. The white-black dashed rectangle marks the frame of the ALOS/PRISM stereo images. The inset panel indicates the geographical location of the study area (black rectangle). The arrow in the inset panel points to the location of the Koxkar glacier, which is mentioned in section 2.3.7.

peripheral forelands in the southern slope are basically controlled by arid climate. The average annual precipitation in the downstream regions of Muzart and Karayulgun rivers is only ~80 mm. Nevertheless, these regions play a significant role in producing meat, commodity grain and cotton, and high quality fruit for Xinjiang, even for the nation. Undoubtedly, glacier meltwater from the Tuomuer-Khan Tengri Mountain Ranges is the base for flourishing farming and animal husbandry. Healthy glacier state in the catchments

Table 1
Early 21st Century Glacier Mass Balance Measurements in the Central Tianshan

Scale of measurements	Glacier/region	Time	Method	Mass Balance (m w.e./a)	Data source
Individual	Suek Zapadniy	2010–2013	In situ measurements	−0.37	WGMS (2015)
	Gregoriev	2006–2007	In situ measurements	−0.25	Fujita et al. (2011)
	Northern Inylchek	1999–2007	Geodetic measurements	−0.57 ± 0.46	Shangguan et al. (2015)
	Southern Inylchek			−0.28 ± 0.46	
	Akshiirak No. 354	2010–2014	In situ measurements	−0.52 ± 0.24	Kronenberg et al. (2016)
		2003–2014	Accumulation and melt model	−0.43 ± 0.09	
		2003–2012	Geodetic measurements	−0.48 ± 0.07	
Subregional	Southern slope of Tuomuer range	1999–2009	Geodetic measurements	−0.23 ± 0.19	Pieczonka et al. (2013)
	Akshiirak range	2000–2013	Volume-area scaling	−0.49~ − 0.59	Petrakov et al. (2016)
Regional[a]	Central Tianshan	2000–2012	Geodetic measurements	−0.21 ± 0.20	Li et al. (2017)
		2003–2009	Laser altimetry measurements	−0.28 ± 0.37	Farinotti et al. (2015)

[a]A glacier mass density of 900 kg/m^3 was used to convert the glacier volume changes into mass balances.

would be refreshing for the settlements in the Muzart and Karayulgun river basins, because the time left for making proper hydrological policy in response to the warming trend is relatively ample. Note that the for the Muzart river, the proportion that glacier meltwater accounts for the total runoff is as high as 56.8% (Duan et al., 2010). Meanwhile, most glaciers in Tianshan belong to the poly-thermal type, which are relatively sensitive to warming (Shi et al., 2008). Our study reveals a rare glacier change phenomenon and indicates that the melting rates of the glaciers can be effectively controlled if the overall rising trend of temperatures, especially the summer temperatures, were reversed. Furthermore, our studies manifest that the glacier change patterns can be highly heterogeneous within a glacial center. When simulating the overall streamflow trend in headwater basin, it is better to calibrate the land surface hydrological model with geodetic method-derived glacier mass balance and to utilize the meteorological data with a spatial resolution as fine as possible.

2. Field Site and Methods

2.1. Field Site

The Tuomuer-Khan Tengri Mountain Ranges are located in the intersection of Kazakhstan, Kyrgyzstan, and China (see Figure 1). As the major glacial center of the CTS (Shi et al., 2008), it gives birth to glaciers with a total area of approximately 3,849.5 km^2 (Su et al., 1985). The moisture in the Tuomuer-Khan Tengri Mountain Ranges is mainly brought by the prevailing westerlies. For glaciers in this area, a year can be divided into two seasons—summer and winter—with the former lasting from around May to September. About 70% of the total precipitation in this area occurs in summer (Ren, 1990). Therefore, both accumulation and ablation of glaciers converge in the summer. The glacierized area of interest is located at the furthest southeast part of the Tuomuer-Khan Tengri Mountain Ranges (see Figure 1), belonging to the catchments of Karayulgun and Muzart rivers. Two glacial centers are covered by the employed ALOS/PRISM stereo images. These glacial centers are divided by a deep valley (the Muzart River) running from the northwest to the southeast. The two glacial centers present distinct characteristics of glacier length/area, orientation, accumulation area ratio, and debris coverage. Therefore, the following analyses were implemented separately for the two glacial centers. Except for the glacier surfaces, no open flat zones can be found. Hence, the terrain mapping is challenging.

2.2. Data

2.2.1. ALOS/PRISM Stereo Images

Launched on 24 January 2006, by Japan Aerospace Exploration Agency (JAXA), the ALOS carries an optical stereo mapping sensor, that is, the PRISM, which is expected to obtain highly precise DEMs. The PRISM consists of three panchromatic cameras pointing in the forward, nadir, and backward directions, respectively. The forward- and backward-looking cameras, each with a 23.8° tilt from the nadir, realize an along-track base-to-height ratio (B/H) of 1. The standard DEM acquisition mode, that is, the triplet mode, takes images from three directions with a swath width of 35 km and a nadir resolution of 2.5 m in a single track. Due to the look angle difference, the coverage of the forward image slightly shifts from that of the backward image. In this study, level L1B1 (only radiometric calibration is performed) triplet stereo images (forward, nadir, and backward looking) acquired on 29 August 2010 (path: 513, frame: 830) were employed to derive the new DEM (see Table 2). Figure 2 displays the forward and backward images covering our study area. Some cloud can be discerned in the low parts of the two polygons (see the right part of Figure 2).

2.2.2. ICESat/GLAS Land Elevation Product

The ICESat was launched in January 2003 by NASA. The primary purpose of the onboard GLAS is to obtain a decimeter-level accuracy for the elevation measurements over ice sheets, sea ice, ice caps, and glaciers (Schutz et al., 2005). Apart from measuring ice thickness changes, the global sampling of surface elevation with an unprecedented high vertical accuracy (1–4 cm for flat areas and approximately 4–13 cm per degree of slope) enables the ICESat/GLAS products to serve as a validation reference for archived DEMs (Berthier & Toutin, 2008) and a height control source for newly generated DEMs (Atwood et al., 2007; Nuth & Kääb, 2011; Pieczonka et al., 2013). In this study, the ICESat/GLAS GLA14 land elevation product (release 33) over stable areas was employed as the vertical control for the ALOS/PRISM stereo model computation (see Figure 2). For a rational comparison with the SRTM DEM, the GLA14 land elevation product was transformed from the TOPEX/Poseidon ellipsoid to the WGS84 and EGM96 reference system.

Table 2
Images Used in This Study

Image	Date	**Path/frame** (for ALOS); **Path/row** (for Landsat); **Item ID/scene no.** (for TanDEM-X)	Scene ID	**Cloud** (for Landsat); **Perp. baseline** (m; for TanDEM-X and ALOS/PALSAR)
ALOS/PRISM L1B1	29 Aug. 2010	181/2700	ALPSMF244792700	1.5%
		181/2755	ALPSMN244792755	
		181/2810	ALPSMB244792810	
Landsat-7/ETM+ L1T	5 Aug. 2000	146/31	LE71460312000218SGS00	0.7%
	18 Aug. 2002	147/31	LE71470312002230SGS00	7.0%
	5 Oct. 2002	147/31	LE71470312002278SGS00	1.2%
Landsat-8/OLI L1T	10 Jul. 2014	147/31	LC81470312014191LGN00	6.7%
TanDEM-X/CoSSC	3 Mar. 2012	1057074/3	PID_TDM-CoSSC-DEM:/dims_ op_pl_dfd_XXXXB00000000293549870023/ dims_op_pl_dfd_//TDM.SAR.COSSC	168
	25 Mar. 2012	1055825/3	PID_TDM-CoSSC-DEM:/dims_op_pl_dfd_ XXXXB00000000293892722086/ dims_op_pl_dfd_//TDM.SAR.COSSC	166
ALOS/PALSAR	20 Dec. 2006	513/830	ALPSRP048230830	660
	4 Feb. 2007	513/830	ALPSRP054940830	

2.2.3. SRTM DEM

The newly distributed 1 arc-second SRTM DEM was adopted as the benchmark elevation. The SRTM DEM is a global DEM acquired within 11 days in February 2000. The nominal relative and absolute vertical accuracies of the SRTM DEM are 6 and 16 m, respectively, and the corresponding horizontal accuracies are 15 and 20 m, respectively (with a 90% confidence level) (Rabus et al., 2003). Rodríguez et al. (2006) reported that 90% of the Eurasia SRTM DEM has absolute horizontal and vertical accuracies of 8.8 and 6.2 m, respectively. In this study, we extracted the SRTM elevations at location ICESat/GLAS GLA14 points via bilinear interpolation and subtracted them from the GLA14 elevations. The mean and root mean square error of the difference were 3.08 and 8.06 m, respectively. Due to the data acquisition consistency, extensive coverage, and promising accuracy, the SRTM DEM is deemed an excellent benchmark for glacier thickness change measurements in midlatitude areas. The distributed data have already been referenced to the WGS84 datum and EGM96 geoid. For our study area, the original 1 arc-second is equal to ~23.0 and ~30.9 m in the east and north directions under UTM projection (zone 44°N), respectively. Before differencing with the new DEM, the SRTM DEM was projected to WGS84 UTM coordinates (zone 44°N) and oversampled to a 15-m resolution.

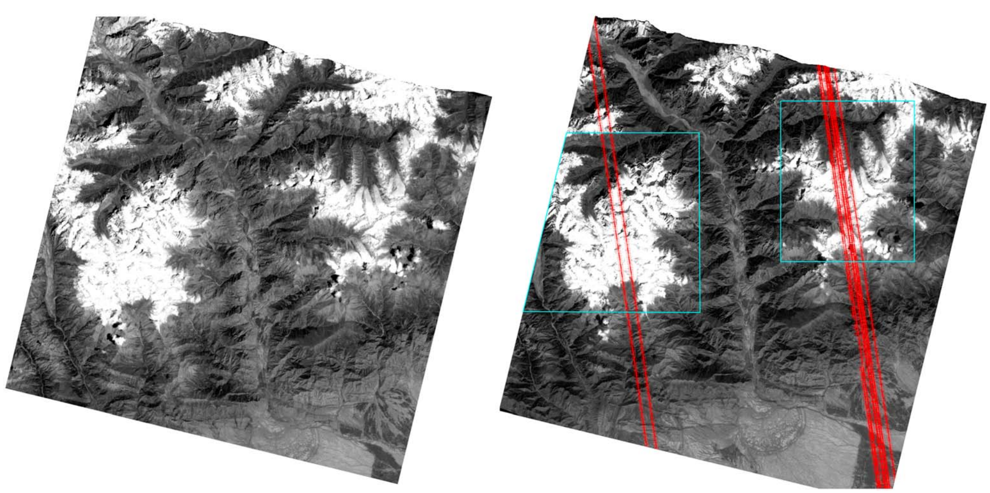

Figure 2. ALOS/PRISM backward- (left) and forward- (right) looking images. In the forward image, the red crosses in lines denote the ICESat/GLAS tracks. The left and right cyan polygons mark the west and east glacial areas that are studied in this paper, respectively.

2.2.4. Landsat/ETM+ Images

The Landsat-7/ETM+ level L1T images distributed by the USGS were employed to delineate the glaciers and provide horizontal control. Note that the L1T images had been orthorectified using GCPs collected from the Global Land Survey data set. Referring to the metadata file, about 190 GCPs were used for a standard ETM+ image, and a geometric model with a root mean square error of about 4 m was achieved. In terms of horizontal accuracy, the Landsat-7/ETM+ level L1T images are compatible with the SRTM DEM since the latter is employed as the DEM source for the Landsat-7 ETM+ image geometrical correction (Nuimura et al., 2015). In our study area, the relief features in the Landsat-7/ETM+ L1T images and the SRTM DEM overlap very well, indicating that the Landsat-7/ETM+ level L1T images are qualified to serve as the horizontal control source (Pieczonka et al., 2013). Furthermore, collecting GCPs from orthorectified images (15 m resolution) other than topographic maps (usually 1:25,000–50,000) decreases the possibility of mistargeting. A Landsat-7/ETM+ image acquired in the ablation season (5 August) of 2000 was available (path: 146, row: 31) in our study area. Sharing the same acquisition year as the SRTM DEM, this image is of significant value for glacier volume change estimation. However, some seasonal snow and cloud can be discerned in this image. In order to minimize the effect of cloud, relief shade, and seasonal snow and to revise the outlines of the glaciers that advanced or surged during our observation period, other images acquired on 18 August 2000, 5 October 2002, and 10 July 2014 (path: 147, row: 31) were also employed (see Table 2).

2.2.5. TanDEM-X/CoSSC Images

InSAR can work regardless of clouds and brightness contrast on the ice/snow surface. The SRTM DEM was derived by single-pass InSAR over the course of 11 days. Its success is down to the excellent coherence assured by the synchronous acquisition of master and slave images. With regard to the great demand for a new global DEM, in 2010, the German Aerospace Center (DLR) launched a new InSAR mission that consists of two satellites: TerraSAR-X (TSX) and TanDEM-X (TDX). The new global DEM is to be derived via an innovative two-pass interferometric mode; that is, either TSX or TDX transmits a microwave signal, while the scattered echo is recorded by both satellites simultaneously. This interferometric mode not only can work independent of glacier motion and atmospheric disturbance but also can achieve excellent image coherence. Therefore, the relative vertical accuracy of the new global DEM is expected to be fairly high, that is, 1–2 m (in the case of a 24-m resolution; Hajnsek et al., 2010). In this study, we adopted StripMap TanDEM-X CoSSC (coregistered slant range single look complex) images that were used for generating the new global DEM. The StripMap TanDEM-X image has a ground range and azimuth resolution of 1.7–3.5 (corresponding to a 45–20° incidence angle) and 3.3 m, respectively. An image can cover a swath of ~30 × 50 km. The images for the west and east glacial areas of interest were taken on 3 March 2012 and 25 March 2012, respectively (see Table 2).

2.3. Methods

2.3.1. Glacier Delineation

In this study, the simple and robust band ratio method was adopted to delineate the glaciers and build a mask (Paul et al., 2015). By setting a threshold on the ratio of the band 3/band 5 digital numbers (DNs) and an additional one on the band 1 DNs, we could classify the surface features in the Landsat-7/ETM+ level L1T images into two types: glacier and nonglacier. The combination of the band 3/band 5 DN ratio and band 1 DNs has the advantage of being able to map glaciers in cast shadow. Optimal thresholds were determined with the criterion that the result should incorporate as many glaciers as possible, while the noise is still low (Paul et al., 2015). The surface features with band ratios and band 1 DNs higher than the thresholds were classified as ice/snow. After a low-strength median filtering, the binary maps exported from the preliminary classification were converted into polygon vectors for post-editing (outline correction and subbasin division). In the vector domain, it is convenient to remove most of the noise, such as seasonal snow packs, via setting a size threshold for the polygon vectors (e.g., 0.05 km^2). Overlapping the vector layer of the outlines (5 August 2000) and the multispectral panchromatic fused images (18 August 2002, 5 October 2002, and 10 July 2014) can facilitate the correction of the errors caused by seasonal snow, cloud, and deep shadows (Kääb, 2005). For mountain glaciers that are mainly nourished by avalanches and flanked by two ridges, the low reaches are usually covered by debris. Automatic optical classification cannot tell the difference between debris and rocks and therefore needs to be manually corrected based on visual interpretation (Racoviteanu et al., 2009) and DEM assistance. Basically, supraglacial debris has a loose and rugged surface because of the presence of ice cliff/fall, uneven ablation, and the underlying ice flow. In contrast, proglacial moraine (unsorted till) and outwash plain sediment (sorted till) appear compacted and smooth. Meanwhile, the supraglacial debris of an entire glacier tongue usually has similar spectral properties distinct from that of the proglacial till. Furthermore, according to Paul et al. (2004) and Kääb (2005), the areas with slopes below a threshold (e.g., 23°) and in direct connection with clean ice can be considered as debris-covered ice. Finally, referring to the latest Chinese Glacier Inventory (2.0; Guo et al., 2015), we divided the glacial area into individual glaciers (see Figure 1).

2.3.2. Glacier Flow Velocity Measurement

In order to assist the interpretation of glacier mass change patterns, glacier flow velocities were derived from two ALOS/PALSAR images via SAR offset tracking with removal of topographic effects (Li et al., 2014; Sansosti et al., 2006). As we know, the image-matching window can directly affect the results (Strozzi et al., 2002). In theory, if the matching window size reduces within a certain range, the accuracy of computed offsets improved as the proportion of noise rises. Therefore, use of multilevel windows is preferable. In this study, three levels of offset-tracking window sizes were used in succession (48 × 144, 64 × 192, and 80 × 240). An offset-tracking cross-correlation coefficient threshold should be set to guarantee result accuracy. In this study, multiple experiments manifested that use of a cross-correlation coefficient threshold of 0.25 maintained a fine balance between number of outliers and spatial coverage of observations. The final offsets are then determined by cross-correlation coefficient weighted averages of the offsets tracked by different matching windows and the average displacement velocities by dividing the offsets by the image pair interval. Offset tracking computed the initial offsets in two directions (azimuth and line of sight). Assuming the glaciers just flow parallel to their surface, the north and east velocities were estimated from the azimuth and line of sight ones (Li et al., 2014; Luckman et al., 2007).

2.3.3. DEM Generation

DEM generation was conducted within the PCI Geomatica 2014 package. First, GCPs were collected for absolute orientation. The ICESat/GLAS GLA14 product was converted into point vectors and overlapped with the Landsat-7/ETM+ L1T images and the SRTM DEM, respectively. For each ICESat/GLAS footprint outside the glacier mask, the corresponding SRTM elevation was extracted through bilinear interpolation (Kääb et al., 2012). Since the accuracy of ICESat/GLAS GLA14 data is uneven, only the points with differences between GLA14 and SRTM of less than 6 m were picked as GCPs. The User Guide of PCI Geomatica OrthoEngine recommends 10–15 GCPs per image for PRISM stereo model computation. In our study, 15 stereo GCPs were collected, with consideration of the necessity for an even distribution. Meanwhile, over 100 evenly distributed tie points corresponding to ground features, such as horns, ice crevasses, river confluences, and rocks, were collected for relative orientation. The residual errors at the GCPs were around 1.5 m. After the orientation, a quasi-epipolar image pair was created, and subpixel image matching (cross-correlation) was performed. Finally, the DEM was generated by converting the parallax to height based on the stereo model. Compared to SPOT/HRS (0.8) and ASTER (0.6) stereo images, the PRISM forward-backward stereo images have a higher B/H ratio (1.0), which can increase their sensitivity to topography. However, the higher B/H ratio can also cause stronger stereoscopic distortion in rugged areas, which leads to failures in the image matching (Berthier & Toutin, 2008). In this case, we opted to combine the nadir image with the forward and backward ones, respectively. Hence, two DEMs were generated. On the one hand, the B/H ratio (0.5) is lower than that of the forward-backward combination. On the other hand, the observation samples are substantially increased. As for the DEM pixel size, the choice of a coarse pixel size can decrease the gross errors and limit the occurrence of data holes (Kääb, 2005). Considering the pixel size of the benchmark DEM, we chose 15 m as the new DEM pixel spacing, although the raw PRISM image has a much higher resolution (2.5 m). PCI Geomatica 2014 offers a score map for evaluating the reliability of the generated elevations. On this basis, we excluded the elevations with scores lower than 80. However, the elevation reliability cannot be solely judged by the magnitude of the score (Holzer et al., 2015). In theory, the elevation generation scores of adjacent pixels should not be homogeneous, since ground surface features are inhomogeneous. The distinction between adjacent points is the basis of image matching. When differencing the DEMs, we found that the areas with homogeneous scores usually had wrong elevations, no matter how high the score was. Hence, in the new DEM, the small areas with homogeneous scores were masked. Areas with scores lower than 80 or homogeneous scores are basically pure glacier/snow surfaces or steep hillsides where stereo image matching failed due to severe image distortion or the lack of brightness contrast. In addition, a low-strength median filtering (3 × 3) was performed to remove some wrong matching induced outliers such as spikes and depressions. The new DEM shared the same reference system as the SRTM DEM.

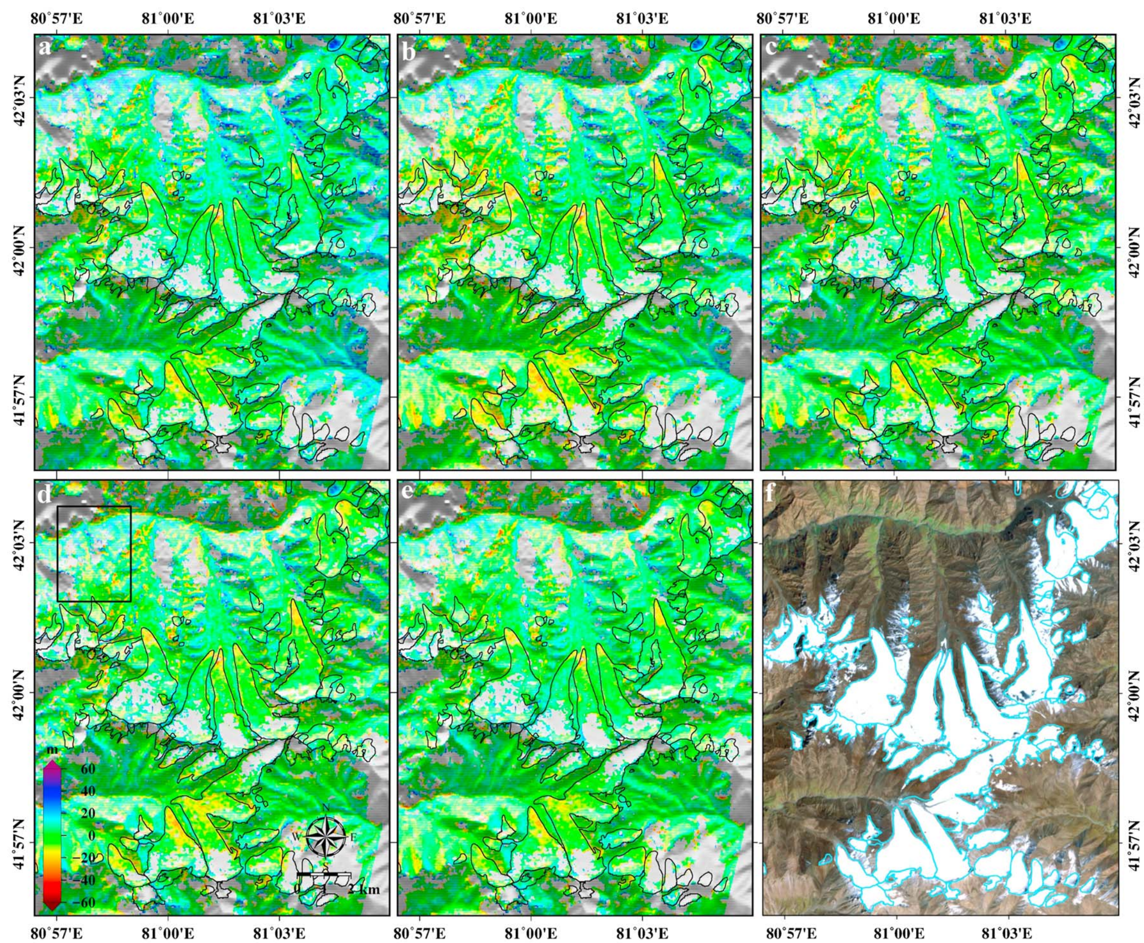

Figure 3. Improvement of the height differences (PRISM DEM-SRTM DEM) over the east glacial area. The PRISM DEM was derived from the nadir-forward stereo image. (a) The raw height difference map. (b) The height difference map after coregistration. (c)–(e) The height difference maps after planimetric, terrain aspect, and curvature-related bias correction, respectively. (f) Landsat image of the east glacial area (fusion of multispectral band combination 321 (RGB) and panchromatic band 8). The base maps of (a)–(e) are the shaded SRTM DEM. The location of the presented area is denoted by the right rectangle in the right panel of Figure 2. The rectangle in (d) marks the area with relatively clear aspect-related bias correction. The black curves in (a)–(e) and slight blue curves in (f) denote the glacier outlines. Gray areas of (a)–(e) are gaps of height difference. The exact magnitudes of the corrections are listed in Table 3.

2.3.4. DEM Co-Registration

Height difference maps were made by subtracting the SRTM DEM from the new PRISM DEMs. The points with absolute height differences larger than 80 m were abandoned (Gardelle et al., 2013). Although the SRTM DEM and PRISM DEMs have the same georeference, their geolocation accuracy may be inconsistent since they are obtained by different sensors and orientation procedures. A small horizontal shift will induce significant elevation differencing errors due to the steep slope in mountainous areas. Therefore, the two DEMs must be coregistered before differencing. Kääb (2005) presented an analytical coregistration method for mountainous DEM differencing. This method is based on the strong relationships between horizontal shift, DEM derivatives (local slope and aspect), and the raw height difference in stable areas (Figures 3a). For more details on this method, refer to Kääb (2005), Nuth and Kääb (2011), and Paul et al. (2015). This method was opted due to its advantage of a fast iteration convergence speed (two to three iterations are enough) and low limit to the proportion that nonglacial height difference samples account for in the whole scene (say 10%; Nuth & Kääb, 2011; Paul et al., 2015). Note that the coregistration was based on raw height differences. Although a considerable number of observations were missed after outlier exclusion, the number of nonglacial height differences was enough to detect the universal systematic bias (see Figures 3a and 4a).

The PRISM DEMs were shifted according to the parameters obtained via analytical coregistration. We adopted the normalized median absolute deviation (NMAD) as the evaluation criterion for the

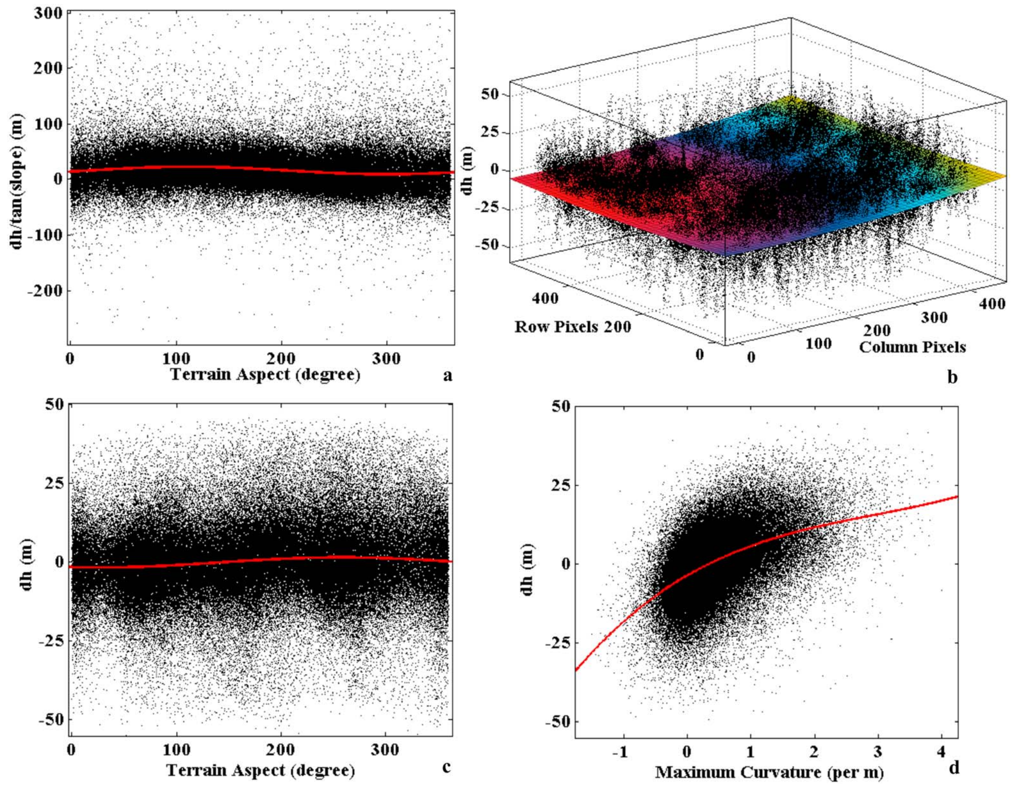

Figure 4. Universal bias trends fitted for the nonglacial height differences of the east glacial area (see Figure 3). (a) Scatterplot between the ratio of the nonglacial height difference over the tangent of the slope (*dh*/tan(slope)) and the terrain aspect (prior to coregistration correction). The red curve denotes the fitted model (cosine function). (b) Three-dimensional view of the scatterplot of the nonglacial height difference versus planimetric positions. The surface denotes the fitted trend using a quadratic polynomial. (c) Scatterplot of the nonglacial height difference versus terrain aspect. The red curve denotes the fitted trend using a first-order Fourier series. (d) Scatterplot of the nonglacial height difference versus maximum curvature. The red curve denotes the fitted trend using a third-order polynomial.

coregistration and for the subsequent bias correction (the reason for this choice is given in section 2.3.9). The nadir-forward height difference map covering the east glacial center was chosen to illustrate the correction effects. The comparison between the height difference maps before and after DEM coregistration is displayed in Figure 3 (a versus b). After coregistration, the mean of the nonglacial height difference was shifted to 0, and most of the singular values on the edge of the glacier were corrected. The NMAD improvement was not so obvious (see Table 3), since among the sources of systematic bias, the planimetric bias (not yet accounted for) has the dominant effect. Nevertheless, the coregistration was nontrivial and fundamental for the following bias correction. Note that the analytical method of coregistration consists of two steps. In the first step, horizontal and vertical shifts are derived via a cosine model fitted between the terrain aspect and the ratio of the height difference over the tangent of the slope (Δh/ tan (slope); Figure 4a). For simplification, the slope-associated vertical shift is deemed as

Table 3
Statistics of the Nonglacial Height Difference Displayed in Figure 3

Height difference map	Median (m)	Mean (m)	STD (m)	NMAD (m)	NMAD improvement (%)
Raw	4.06	4.36	12.47	10.54	—
After coregistration	−0.36	0.00	12.41	10.49	0.5
After planimetric bias correction	−0.31	0.00	11.93	9.87	5.9
After aspect bias correction	−0.24	0.00	11.82	9.66	2.2
After curvature bias correction	0.14	0.00	10.87	8.32	14.3

Note. STD = standard deviation, NMAD = normalized median absolute deviation.

constant. Consequently, the effect of coregistration correction is limited in relatively flat areas but exaggerated in steep ones (Nuth & Kääb, 2011). In order to correct the induced vertical bias, in the second step, a universal trend was fitted between the nonglacial height difference and the tangent of the slope using a first-order polynomial and then removed from the PRISM DEM.

2.3.5. Systematic Bias Correction

After the coregistration correction, the systematic bias related to planimetric position, aspect, and curvature (the first derivative of slope) were examined and corrected. The sources of bias we dealt with are not unique for the case in which the PRISM DEM was employed. Due to the inaccessible and complicated original data acquisition procedures, the determination of a physical model for these sources of bias is very difficult. Therefore, we analyzed and corrected these systematic biases via universal statistical approaches. Based on the assumption that the bias of the glacial and nonglacial height differences is homogeneous, the height difference map can be corrected by removing the universal bias trends fitted from the nonglacial samples (Muskett et al., 2008; Nuth & Kääb, 2011). Such a treatment is simple and effective. Table 3 and Figure 3 show that the glacial height differences become increasingly reasonable after the systematic bias corrections.

2.3.5.1. Planimetric Bias Correction

As mentioned above, the planimetric bias was dominant among the sources of systematic bias and was therefore treated first. In Figure 3b, that is, the height difference map after coregistration correction, a west-east tilted systematic bias can be easily discerned. Similar bias patterns were also detected in Racoviteanu et al. (2007), Peduzzi et al. (2010), Bolch et al. (2011), Pieczonka et al. (2011, 2013), and Willis et al. (2012). The InSAR-derived SRTM DEM may be responsible for this planimetric bias. When differencing the simultaneously acquired C- and X-band SRTM DEMs, we found obvious planimetric trend of image frame scale in the height difference map. Basically, the residual baseline during the retrieval of InSAR height can cause planimetric bias in the final product. Obviously correlated with the horizontal position, this bias was fitted as a universal surface trend using a quadratic polynomial model (Figure 4b) and then removed from the height difference map. After the correction, the NMAD of the height difference on the ice-free areas was improved by 5.9% (Figure 3b versus Figure 3c).

2.3.5.2. Terrain Aspect Related Bias Correction

According to previous studies (Peduzzi et al., 2010; Pieczonka et al., 2011, 2013; Racoviteanu et al., 2007; Surazakov & Aizen, 2006), terrain aspect related bias can affect the height difference maps. When plotting the nonglacial height difference against terrain aspect, we also discerned the dependent relationship between them. A universal bias trend was fitted using a first-order Fourier series (Figure 4c) and then removed from the height difference map. Such aspect-related bias was also reported in Kääb (2005). Both the GCP location and the foreshortening caused by the slant-range image geometry of the SRTM DEM might account for this bias. After correction, the NMAD of the height difference on the ice-free regions was improved by 2.2% (Figure 3c versus Figure 3d).

2.3.5.3. Curvature-Related Bias Correction

Paul (2008) pointed out that the distinction between the original resolutions of the two DEMs employed for differencing could also induce bias. More precisely, the elevations of the coarse DEM are likely to be underestimated when the curvatures are high. To reach the 15-m resolution, the PRISM image and SRTM DEM needed to be downsampled and oversampled, respectively. Therefore, curvature-related bias was also discerned in our height difference map. At the mountain ridges, cirque walls, and ice falls, the positive height differences took up a larger proportion (see Figure 3d). According to Gardelle et al. (2012b, 2013), the maximum curvature can be used to fit this bias (relative to plan curvature). A universal bias trend was fitted using a third-order polynomial (see Figure 4d) and then removed from the height difference map. Note that the maximum curvature for fitting was extracted from the PRISM DEM that had been corrected by the previous steps. After correction, the NMAD of the height difference over the ice-free regions was improved by 14.3% (Figure 3d versus Figure 3e).

2.3.6. Penetration Correction

The C-band microwave applied by the SRTM can penetrate into snow, firn, and ice (Rignot et al., 2001) and can therefore result in elevation underestimation. Basing on the hypothesis that X-band microwaves possess a much weaker penetration capability than C-band microwaves, Gardelle et al. (2012a) and Pieczonka et al. (2013) estimated the depth of C-band penetration in snow/ice via differencing the simultaneously acquired C-band and X-band SRTM DEMs. Using this approach, we derived an average C-band penetration depth of 2.7 m in the CTS. Prior to our study, Karakoram, Bhutan, and East Nepal-Bhutan were reported to have C-band

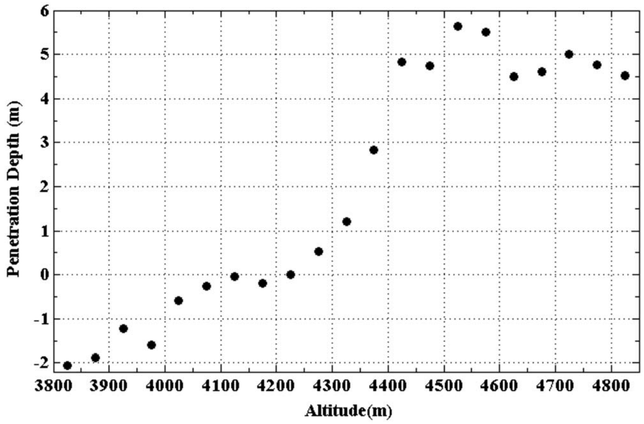

Figure 5. C-band microwave penetration depth into the glacier surface within our study area. Each solid circle denotes the average penetration depth within an altitude interval (50 m).

penetration depths of 2.4 (Kääb et al., 2012), 2.4 (Gardelle et al., 2013), and 2.5 m (Kääb et al., 2012), respectively, which are similar results to ours. Furthermore, by extrapolating the robust linear regression of the mean differences between the C-band SRTM and 2003–2009 ICESat/GLAS GLA14 elevations, Pieczonka and Bolch (2015) obtained a C-band penetration depth of 2.2 m for the CTS. We took the difference between our measurement and that of Pieczonka and Bolch (2015), that is, 0.5 m, as the uncertainty of the penetration depth. In order to present a thickness change map less biased by penetration and to compute the thickness changes of the ablation and accumulation zones separately, we applied the penetration depth correction to each pixel by fitting as a function of the altitude (Gardelle et al., 2013). Our penetration depth's distribution with respect to altitude (see Figure 5) tallies with the conclusion of Berthier et al. (2006); that is, the C-band SRTM elevations are 2 m higher in the lower ablation zones and 5–10 m lower in the higher accumulation zones than they should be.

2.3.7. Seasonal Correction

The ALOS/PRISM stereo images were acquired in a different season than the SRTM DEM (August versus February). In order to count the observation period as 11 years (from February 2000 to February 2011), 4.5 months of winter mass balance and 1 month of summer (May to September) mass balance should be added to the geodetic measurement result. Based on the degree-day mass balance model constrained by glacier surface precipitation and temperature observations, Zhang et al. (2006) reported that the annual mass balance values of 2003/2004 and 2004/2005 over the Koxkar glacier were −494 and −384 mm w.e., respectively, and the summer mass balance values in 2004 and 2005 were −847 and −925 mm w.e., respectively. The Koxkar glacier is located in the southwest of the Tuomuer-Khan Tengri Mountain Ranges (see Figure 1). To the best of our knowledge, it is the nearest glacier with reliable seasonal mass balance records. We therefore took the averages for the correction, that is, a summer month mass balance of −177 mm w.e. and a winter month mass balance of 64 mm w.e.

2.3.8. Glacier Mass Balance

The original SRTM DEM has tiny data gaps over the studied glaciers, which can be seen in the thickness change maps based on the TanDEM-X DEM (introduced in section 4.2). The voids in the thickness change map were mainly caused by failures in the ALOS/PRISM elevation generation. If a void-filled height difference map was exported, the interpolated samples with much lower accuracy would significantly bias the results. We preferred the noninterpolated map since void observation is better than unreliable ones. In fact, the glacier ablation zones where major thickness changes occurred were well observed. In this case, the hypsography method was adopted for calculating the glacier volume changes, that is, multiplying the average thickness difference and the total glacier area in each elevation interval (50 m) and then summing all the products (Kääb, 2008). The areas without thickness change measurements were given the average thickness change of the altitude range they locate in (Gardelle et al., 2013). In comparison to the glaciological or ICE/GLAS measurements, our measurements have a much higher sampling density. The hypsography was determined by the SRTM-TanDEM fused DEM and glacial mask. To convert the volume changes to mass balance, a mass density should first be determined. Previous studies have taken two different density choices. The first choice is to assign a density of snow/firn (say 550 kg/m^3) and ice (900 kg/m^3) to the mass below and above the snowline, respectively (Schiefer et al., 2007; Tennant et al., 2012; Willis et al., 2012). The second choice is to use the ice density as the overall glacier density (Berthier et al., 2010; Gardelle et al., 2012a, 2013; Pieczonka et al., 2013; Pieczonka & Bolch, 2015). In this paper, considering that the accumulation zone thickness changes were slight and in order to facilitate a comparison with other measurements, we adopted the latter approach. However, the difference with the former approach was considered as an uncertainty source (discussed below).

2.3.9. Uncertainty Analysis of Glacier Mass Estimation

In this study, we considered three sources of uncertainty for the glacier mass estimation, that is, glacier outline delineation uncertainty, glacier thickness change uncertainty, and glacier density uncertainty. Due to the limit of the Landsat-7/ETM+ multispectral panchromatic fused image zoom level during the post-editing, we

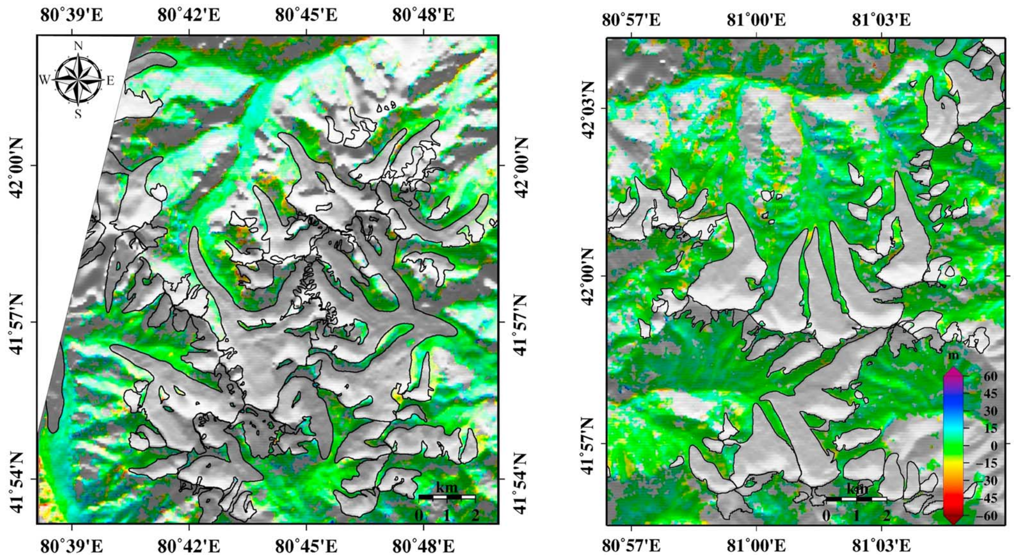

Figure 6. Nonglacial height differences between Shuttle Radar Topography Mission (SRTM) digital elevation model (DEM) and PRISM DEM within the west (left) and the east (right) glacial centers. The black curves denote the glacier outlines. Base maps are shaded SRTM DEMs.

assumed an uncertainty of one image pixel, that is, 15 m, for the glacier delineation (Hagg et al., 2013). This delineation uncertainty corresponded to a glacier area deviation of ±7.7% for the west and ±8.6% for the east glacial centers. However, the corresponding mass balance uncertainties were only ±0.004 and ±0.003 m w.e./a for the west and east centers (counting the observation time as 11 years), respectively, and therefore negligible. Furthermore, a different density choice led to a mass balance uncertainty of ±0.003 m w.e./a for both the west and east centers, which was also negligible.

Glacier thickness change uncertainty is the major uncertainty source for mass balance estimation. Basically, the accuracy of the new DEM is affected by the B/H ratio, the GCP quality, and the image matching error (Pieczonka et al., 2011). The absolute DEM error is usually evaluated by checking the elevation difference (root mean square error) relative to independent GCPs or a DEM derived by a highly reliable technique. However, in terms of glacier thickness change measurement, the significance of the relative errors of the two DEMs outweighs that of the absolute error, since the former represents the accuracy of the elevation differences while the latter denotes DEM control with respect to a datum (Cox & March, 2004). As shown in Figures 3e and 6, most nonglacial height changes were close to 0, indicating that the two vertical reference systems of the SRTM DEM and PRISM DEM were consistent.

Assuming that the height difference errors in the glacierized and ice-free regions are common, we can describe the glacier thickness change errors using the mean and standard deviation (STD) of the nonglacial height differences. The former denotes the systematic shift between the two DEMs, and the latter reflects the dispersion of the observations from their mean. Hence, the STD is supposed to be the evaluation criterion for bias correction. However, the STD computed in the normal way is sensitive to outliers. Höhle and Höhle (2009) pointed out that when the number of outliers is considerable, the NMAD can be an alternative estimator for scaling the height difference and is computed by the following:

$$\mathrm{NMAD} = 1.4826 \cdot \mathrm{median}\left(\left|\Delta h_i - \mathrm{median}_{\Delta h}\right|\right) \tag{1}$$

where Δh_i is the nonglacial height difference. The NMAD is proportional to the median of the absolute difference between Δh_i and the median of the nonglacial height difference. Referring to Pieczonka et al. (2013), Pieczonka and Bolch (2015), and Holzer et al. (2015), we regarded the nonglacial height differences lying beyond the two-tailed 1.5 times interquartile range (acquired by subtracting the 25% quantile from the 75% quantile) as outliers and removed them. The STD and NMAD computed before and after outlier removal (listed in Table 4) indicate that the NMAD can be deemed as an estimator of the STD that is less sensitive to outliers, and in the case of a normal distribution, the former is close to the latter. Therefore, we adopted the

Table 4
Standard Deviation (STD) and Normalized Median Absolute Deviation (NMAD) of the Nonglacial Height Differences Before and After Outlier Removal

Glacial area	Before outlier removal			After outlier removal		
	STD (m)	NMAD (m)	STD of the mean (m)	STD (m)	NMAD (m)	STD of the mean (m)
West	±10.81	8.74	±0.19	±7.53	7.69	±0.14
East	±8.95	7.48	±0.16	±6.48	6.68	±0.12

NMAD as the evaluation criterion for bias correction. The nonglacial STDs after outlier removal were ±7.53 and ±6.48 m for the west and east glacial area, respectively, which are comparable to the results obtained in previous studies acquired by subtracting the SRTM DEM from the 2009 SPOT5/HRG DEM (±8.4 m; Pieczonka et al., 2013) or the 2008–2011 SPOT5/HRS DEM (±5.20 to ±14.84 m; Gardelle et al., 2012a). Note that our study area is purely mountainous, while that in Pieczonka et al. (2013) and Gardelle et al. (2012a) included open forelands. Furthermore, we did not set any slope thresholds for the statistics of the height differences.

Since the results represent the average changes of the whole glacierized area, the nonglacial STD is an overestimated estimator for scaling thickness change uncertainty. Therefore, previous studies (Bolch et al., 2011; Cox & March, 2004; Gardelle et al., 2012a, 2013; Kääb, 2008; Koblet et al., 2010; Nuth & Kääb, 2011; Willis et al., 2012) have adopted the STD of the mean (S_ε) as the estimator, which can be calculated by the following:

$$
\begin{aligned}
S &= \sqrt{\frac{1}{n-1}\Sigma_{i=1}^{n}\left(\Delta h_i - \widehat{\mu}\right)^2} \\
S_\varepsilon &= \frac{S}{\sqrt{N}}
\end{aligned}
\tag{2}
$$

where n and $\widehat{\mu}$ are the number and mean of the nonglacial height difference samples, respectively. To some degree, the samples of the DEM are spatially autocorrelated. N stands for the number of spatially uncorrelated samples. Provided that the DEM is uncorrelated over a certain length, N can be calculated as follows (Gardelle et al., 2012a):

$$
N = \frac{\rho n}{2d} \tag{3}
$$

where ρ and d are the DEM pixel size and the autocorrelated length, respectively. For 30-m DEMs, we determined 600 m (i.e., 20 pixels) to be the autocorrelated length (Bolch et al., 2011; Koblet et al., 2010). The S_ε of the west and the east areas were ±0.14 and ±0.12 m, respectively (see Table 5). Clearly, S_ε decreases as the number of nonglacial height differences increases; that is, it is prone to being underestimated.

3. Results

3.1. Glacier Thickness Changes Based on Photogrammetry

The glacier areas delineated for the mass balance measurement were 88.7 and 54.6 km^2 for the west and east glacial centers, respectively (see Table 5). The final glacier thickness changes are the score (measure of the DEM quality offered by PCI) weighted average of the nadir-forward and nadir-backward glacial height changes. Figure 7 presents the derived glacier thickness changes for the two glacial centers. Most areas show smooth and moderate thickness changes, except for the glacier feet and the surge-associated parts. For the west and east centers, 53.0% and 73.4% of the glacier surface has effective thickness change measurements, respectively. The average glacier thickness changes of the west and east glacial centers measured between February 2000 and August 2010 are −0.48 and −0.89 m, respectively. The regional glacier snowlines were computed from

Table 5
Glacier Changes Measured Between February 2000 and August 2010

Index	West glacial center	East glacial center
Snowline (m a.s.l.)	4,219	4,263
Studied glacial area (km^2)	88.7	54.6
Accumulation area ratio	0.61	0.40
Thickness change measurement coverage	53.0%	73.4%
Ablation zone thickness change (m)	−1.04 ± 0.18	−1.59 ± 0.18
Accumulation zone thickness change (m)	−0.14 ± 0.18	+0.22 ± 0.18
Average thickness change (m)	−0.48 ± 0.18	−0.89 ± 0.18
Volume change (km^3)	−0.04 ± 0.02	−0.05 ± 0.01

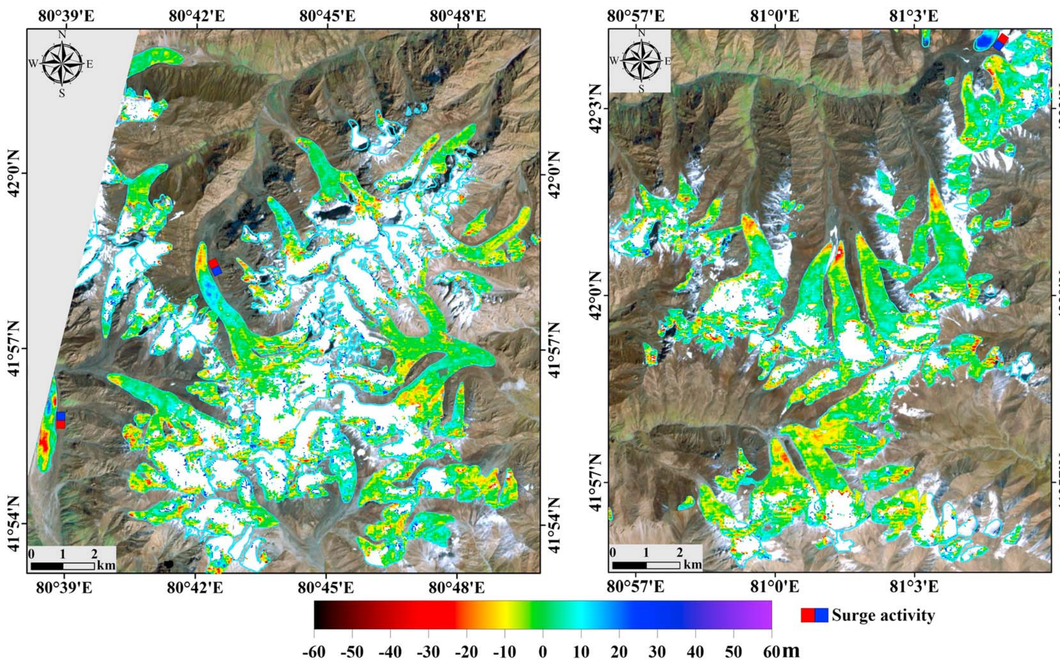

Figure 7. ALOS/PRISM image derived thickness change maps of the west (left) and east (right) glacial centers (February 2000 to August 2010). The light blue curves denote the glacier outlines. White areas within glacier outlines are gaps of thickness change. Surge activity recognition refers to our observations only. Base maps are Landsat images (fusion of multispectral band combination 321 (RGB) and panchromatic band 8).

the given individual glacier snowlines in the China Glacier Inventory via area-weighted averaging. In the west center, the glacier areas above and below the snowline (4,219 m), that is, the accumulation and ablation zones, experienced an average thinning of −0.14 and −1.04 m, respectively. In the east center, the glacier area below the snowline (4,263 m) experienced an average thinning of −1.59 m, while that above the snowline experienced a thickening of +0.22 m. After seasonal correction, the mass balance values of the west and east glacial centers were −0.03 and −0.06 m w.e./a, respectively. For the west glacial center (Figure 7 left), it is apparent that the glaciers in the two sides of the central mountain range experienced quite distinct changes. Thickening could be found not only in the accumulation zones but also in the ablation zones in the west side, while thinning dominated the ablation zones in the east side, even for the parts covered by debris. As for the east glacial center (Figure 7 right), the thickness change patterns were more uniform. Except for the two surge glaciers in the northeast corner, most of the glaciers showed significant thinning in the tongues. From feet to head, the thinning gradually turned into thickening.

3.2. Comparison With the Measurements Based on InSAR and Altimetry

A comparison with field measurements is the direct and convincing way to assess the reliability of our results. However, as mentioned at the beginning, field measurements are difficult to obtain due to the remote location and hostile environment. We therefore adopted another geodetic measurement based on InSAR to evaluate our results. Technically, the InSAR-based geodetic measurements can be persuasive references (Berthier et al., 2016), because the working principle of InSAR is totally different from that of photogrammetry. Two new DEMs were extracted from TanDEM-X CoSSC images via the differential InSAR method, in which the SRTM DEM was employed as the external DEM. The generated DEM had relative elevations and shared the same geographical reference as the SRTM DEM. However, it is the height difference between the SRTM DEM and the new DEM that we require. We also improved the height difference map by removing the universal bias trend fitted from nonglacial samples. Note that the derivation of the InSAR height difference map did not require GCPs. The geolocation of the new TanDEM-X DEM was determined by coregistration between the TanDEM-X image and the SRTM DEM simulated radar image, which can be as accurate as 1/10 pixel.

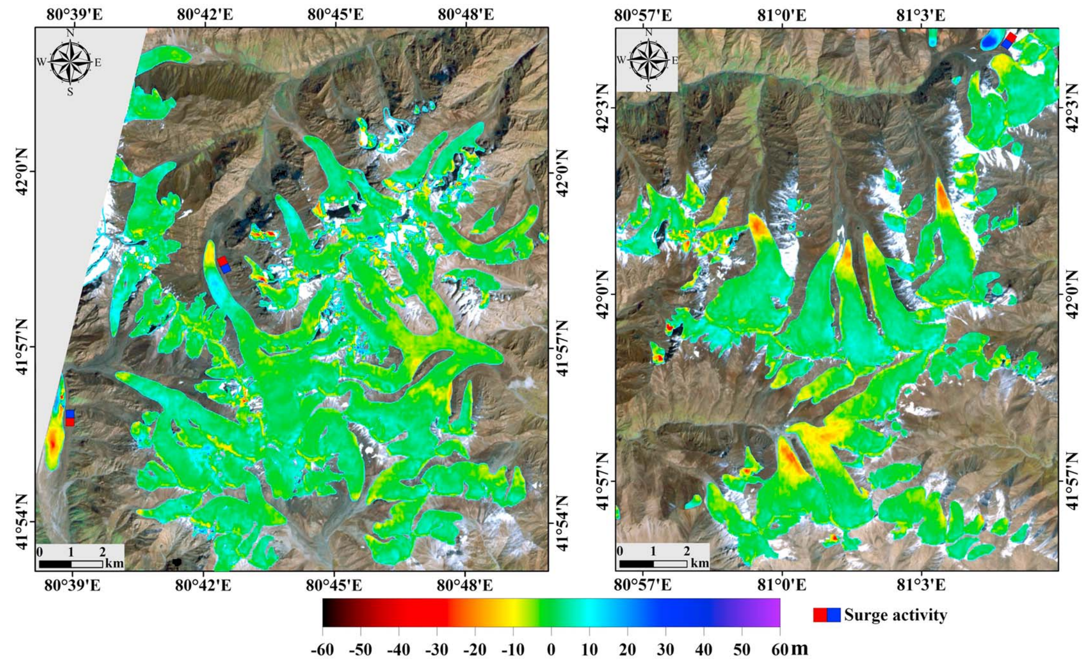

Figure 8. TanDEM-X image derived thickness change maps of the west (left) and east (right) glacial centers (February 2000 to March 2012). The light blue curves denote the glacier outlines. White areas within glacier outlines are gaps of thickness change. Surge activity recognition refers to our observations only. The base maps are Landsat images (fusion of multispectral band combination 321 (RGB) and panchromatic band 8).

The InSAR-derived thickness change maps are presented in Figure 8. When combined with Figure 7, we can discern that the glacier thickness change patterns derived by the two different methods are highly similar. The InSAR thickness change map is also dominated by neutral (close to zero) changes. Only the surge activities and the ablation of the lowest exposed ice caused significant thickness changes. To facilitate the comparison, we plotted the thickness changes against altitude. As shown in Figure 9, in general, the photogrammetry thickness changes are more negative than those of InSAR. The seasonal variability of glacier ablation/accumulation could be the major reason for this. If the observation period is counted from February 2000 to February 2011, mass accumulation should be added to the photogrammetry results. The discrepancies between the two kinds of thickness change distribution mainly appear at the lower altitudes where major ablation occurred. For the east and west glacial centers, the correlations between the two kinds of thickness change distribution are 0.94 and 0.71, respectively. The west glacial center saw more distinct

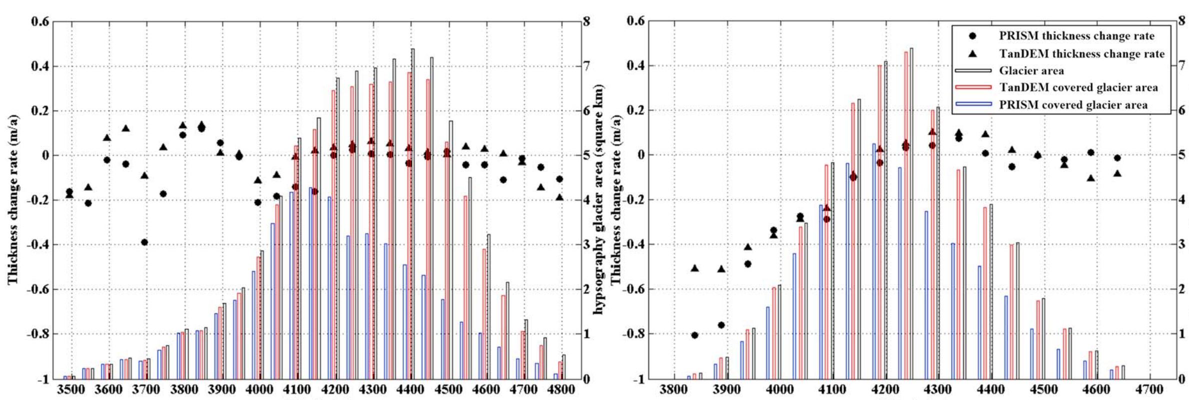

Figure 9. Hypsometry and glacier thickness change rates versus altitude for the west (left) and east (right) glacial centers. Note that the thickness change rate differences contain seasonal and interannual variability.

Table 6
Comparison Between the ALOS/PRISM and TanDEM-X Glacier Mass Balance Measurements

Glacial center	DEM acquisition method, sensors	Period	Thickness change measurement coverage (%)	Mass balance (m w.e./a)
West	Photogrammetry, ALOS/PRISM and	Feb. 2000 to Feb. 2011	53.1	−0.03 ± 0.17
	InSAR, TanDEM-X and SRTM-C	Feb. 2000 to Feb. 2012	94.8	0.01 ± 0.17
East	Photogrammetry, ALOS/PRISM and	Feb. 2000 to Feb. 2011	73.6	−0.06 ± 0.17
	InSAR, TanDEM-X and SRTM-C	Feb. 2000 to Feb. 2012	99.9	−0.04 ± 0.17

discrepancies, since two large glaciers in this area were in surge quiescent phase (the Shuirik and Qungky Zawayi glaciers, see Figure 1). A surge transfers a large volume of glacier mass from a higher reservoir zone to a lower receiving zone. Between two surges, there is a quiescent phase when the reservoir zone regains mass while the receiving zone experiences intense downwasting. Therefore, a surge is associated with remarkable reorganization of the glacier mass (Bhambri et al., 2017; Lønne, 2016; Xie & Liu, 2010). An obvious heightening at the glacier terminus or a tandem combination of marked heightening and lowering is a sign of surge activity, and the interannual and seasonal variability of the ice mass loss rate in the surge quiescent phase can be dramatic. In Figures 7 and 8, the locations of the surge activities are consistent, indicating that these surges occurred between February 2000 and August 2010.

In order to make a rational quantitative comparison, we counted the time periods of the two geodetic measurements from February 2000 to February 2011. Seasonal corrections remained the same as for the measurements based on photogrammetry. Half and one winter month mass balance values were then subtracted from the west and east glacial centers' measurements based on InSAR, respectively. After the seasonal correction, for the east and west glacial centers, the InSAR mass balance values were −0.04 and 0.01 m w.e./a, respectively. The differences between the photogrammetry and the InSAR mass balance measurements were no more than 0.04 m w.e./a, suggesting that our results are reliable. Since the STD and the STD of the mean of the nonglacial height difference derived by the photogrammetry measurements were too high and too low, respectively, we assumed four times the difference between the two measurements as the estimator of the height change uncertainty, that is, the major component of the glacier thickness change uncertainty. In addition, the penetration depth uncertainty and the seasonal correction itself were counted as thickness change uncertainty components. The final mass balance uncertainty, as determined from the delineation uncertainty, the density uncertainty, and the thickness change uncertainty, was ±0.17 m w.e./a, which is a similar level to that reported in Pieczonka et al. (2013; ±0.19 m w.e./a) and Gardelle et al. (2012a; ±0.13 to ±0.18 m w.e./a). We have also subtracted the PRISM DEM from TanDEM-X DEM, and the computed February 2011 to February 2012 glacier mass balances (after seasonal correction) were 0.36 and 0.09 m w.e. for the west and east centers, respectively. According to the glacier mass balance values derived by the photogrammetry and InSAR-based geodetic methods (Table 6), the glacier mass balance between February 2011 and February 2012 should be 0.45 and 0.18 m w.e. for the west and east centers, respectively. In this case, the three measurements are generally consistent, indicating that the uncertainty of mass balance is conservative.

Furthermore, we performed the glacier mass balance measurement based on ICESat/GLAS GLA14 products. Regarding the number of footprints and the acquisition time of each GLAS track, we selected the one on 21 March 2008 for geodetic measurement, which crosses the east glacial center only. A total of 39 points with acceptable quality (no gross errors) were used to determine the glacier thickness change. The height differences at these points range from −15.67 to 8.99 m (GLA14-SRTM DEM, after the correction of C-band penetration). When calculating the February 2000 to February 2008 glacier mass balance based on the hypsography method (with seasonal correction), if we used an altitude interval of 200 m, the result would be −0.05 ± 0.17 m w.e./a, which is very close to the results of photogrammetry and InSAR-based geodetic methods (see Table 6). However, if we narrowed the altitude interval to 100 m, the value would be −0.19 ± 0.17 m w.e./a. The major factors leading to such phenomenon include the small number and the uneven distribution of effective ICESat/GLAS elevation measurements over glaciers. Note that we used the same result uncertainty as photogrammetry and InSAR-based geodetic measurements, because the STD of nonglacial height difference is on the same level (±7.45 m). In general, the glacier mass balance measurement based on ICESat/GLAS GLA14 products agrees with that based on PRISM and TanDEM-X DEMs within uncertainty ranges.

4. Discussion

4.1. Pattern and Mechanism of Glacier Thickness Change

Figures 7 and 9 indicate that the distributions of the glacier thickness changes are not strictly correlated with altitude. For the two glacial centers, the ice thickness change patterns of the ablation zones appear quite distinct. In the east center, the glaciers have little debris coverage. The tongues saw the strongest ice thinning, and the thinning became increasingly weak as the altitude rose. In contrast, in the west center, most of the glacier ablation zones are covered by debris. Furthermore, two of the glaciers in this area belong to the surge type (see Figures 7 and 8). As a result, the thinning rate in the ablation zones are strongly undulated rather than decreased as the altitude increased. However, except for the surge-associated part, it was the lowest exposed ice that saw the strongest thinning. Within the accumulation zones, the ice thickness change patterns of two centers were more uniform. Ascending from the snowline, the thickening first strengthened and soon became increasingly weak. The strongest thickening did not occur in the highest parts, since the headwalls and top cirques are not suitable for storing mass. The mass collected in the highest parts is rapidly transferred to the lower and flatter basins (by avalanche; Li et al., 2014). Note that for the two glacial centers, the measured thickness changes around the snowline are close to zero, which is consistent with the theory that glacier mass input equals output at the equilibrium line (the snowline approximately equals to the equilibrium line at the end of ablation season; Xie & Liu, 2010). In reality, the snowline varies with the mass balance, and the thickness changes are the superimposed effects of decline and ice flow variation. Since none of the glaciers showed surge activity in their middle reaches, this finding indicates that the studied glaciers have hardly changed, which was in accordance with our mass balance measurements.

Although our study area is much smaller compared to that of the High Asia region-wide measurements (Gardelle et al., 2013; Kääb et al., 2012), we can still reveal some mechanisms of mountain glacier thickness change. The two glacial centers are separated by only a valley, which means they may experience similar temperature and solar radiation changes. The factors leading to the obvious discrepancy of thickness change patterns between the two centers include debris cover, glacier geometry, ice thickness, ice temperature, and subglacial hydrological condition. The debris cover plays a significant role on adjusting the glacier surface mass balance. Theoretically, a thick debris cover can attenuate the ice ablation, due to the heat insulation effects (Hagg et al., 2008; Xie et al., 2007). The mountain glacier debris is primarily generated by the scraping during glacier flow and avalanches (Xie & Liu, 2010). Basically, a small altitude drop and a regular-shaped glacier geometry mean slower glacier motion and less frequent avalanches and therefore less debris. For glaciers with little debris cover, receding is the major form of mass loss, because the strongest decline occurs at the terminus. Glaciers at the east center and the south of the west center belong to this kind. For glaciers in the east center, the maximum thinning is supposed to be observed at the glacier terminuses. However, since these glaciers have been receding since before 2000 (Pieczonka & Bolch, 2015), the maximum thinning was found in a slightly higher part (see Figures 7 and 8). In contrast, the debris is much more common over glaciers in the middle and north of the west centers, which have tree-like shapes and flow down from mountains with higher horns/arêtes (see Figure 1). Some of them have a debris coverage larger than 20%. Kääb et al. (2012) and Gardelle et al. (2013) reported earlier that in the Pamir, Spiti Lahaul, Karakoram, and Everst areas, the thickness changes of debris-covered glaciers were similar to that of debris-free glaciers. However, in this study the distinction between debris-covered and debris-free glaciers is sharp. As shown in Figures 7 and 8, the thinning of the debris-covered glacier ablation zones in the east side of the west center is basically 5–10 m slighter than that of the debris-free ones in the east center. Furthermore, the thinning over the debris-covered tongues is uniform, rather than becomes increasingly strong toward the terminus like that over the debris-free tongues, which indicates that the effects of meteorological condition changes were greatly isolated. Due to the debris cover, the glaciers in the west center are able to extend to the altitude 400 m lower than that in the east center. For the large glaciers measured by Kääb et al. (2012) and Gardelle et al. (2013), the effects of debris cover may be significantly counteracted by the effect of englacial drainage system.

Beside debris cover, a glacier's dynamic response to climate change, which is primarily controlled by glacier geometry, ice thickness, englacial temperature, and subglacial hydrological condition, also has significant

10.1029/2017JD028150

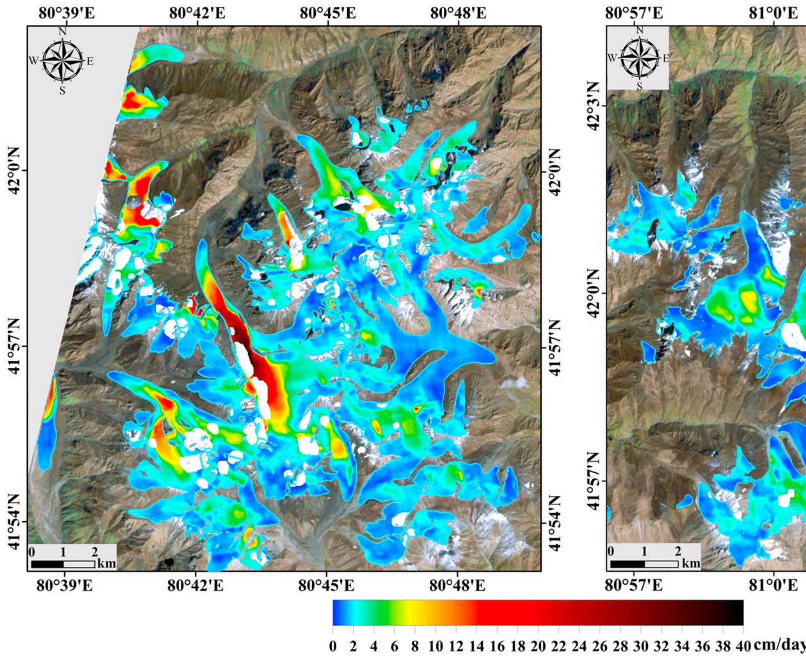

Figure 10. 2-D glacier flow speed of the west (left) and the east (right) glacial centers derived using the offset-tracking technique and ALOS/PALSAR images (20 December 2006 to 4 February 2007). The glacier outlines are denoted by the light blue curves. The base maps are Landsat images (fusion of multispectral band combination 321 (RGB) and panchromatic band 8).

influences on its mass change. For investigating the ice thickness, englacial temperature, and subglacial hydrological condition, the cost is quite high, and therefore, we measured the surface glacier velocity instead, which is highly correlated with these three factors. 2-D glacier flow speed maps (20 December 2006 to 4 February 2007) have been derived using the SAR offset-tracking technique and ALOS/PALSAR images (Li et al., 2014). The surface velocity map is a display of the sensitivities of different glaciers to the external environment changes. Local topography can alter the distribution of moist air carried by atmospheric circulation or monsoon. Therefore, even influenced by the same air current, the glaciers in one center may have various chances of gaining mass. In the west glacial center, there is an approximately north-south orientated mountain ridge. As mentioned in section 2, the moisture in the Tuomuer-Khan Tengri Mountain Ranges is mainly brought by the westerlies. The glaciers lying in the western slope of the mountain, that is, the windward side, have a greater chance of receiving more precipitation. As shown in Figure 10, the glacier flow speeds in the windward and leeward sides of the ridge are contrasting. More precipitation produces a thicker glacier body and therefore faster glacier flow. The higher flow speed in the windward side facilitates the transportation of mass accumulated in the higher reaches. Hence, glaciers in the windward side were more capable of coping with temperature rise and experienced more positive mass changes than glaciers in the leeward side. Combining Figures 9 and 10, we can discern that glaciers with prominent flow velocities even have thickened ablation zones. In the east glacial center, the glaciers mainly lie in a north-south orientation, and their sizes and debris coverage are more uniform. Correspondingly, the glacier decline patterns are more homogeneous. Surge is a special pattern of glacier flow. In theory, the surge itself does not reduce the glacier mass; however, it puts much more mass in “dangerous” places relative to the general glacier flow. In our study area, since most of the surges occurred in the west side of the west center not long ago, we cannot determine whether they have considerable effects on the glacier mass balance. However, our results explicitly manifest that the sharp change of altitude is the prerequisite of mountain glacier surge.

4.2. Reasons for the Anomalous Glacier Changes

In order to corroborate the “anomalous” state of studied glaciers, we collected some clues from previous studies. Li et al. (2017) derived the regionwide CTS glacier thickness change over 2000–2012 using TanDEM-X

Journal of Geophysical Research: Atmospheres 10.1029/2017JD028150

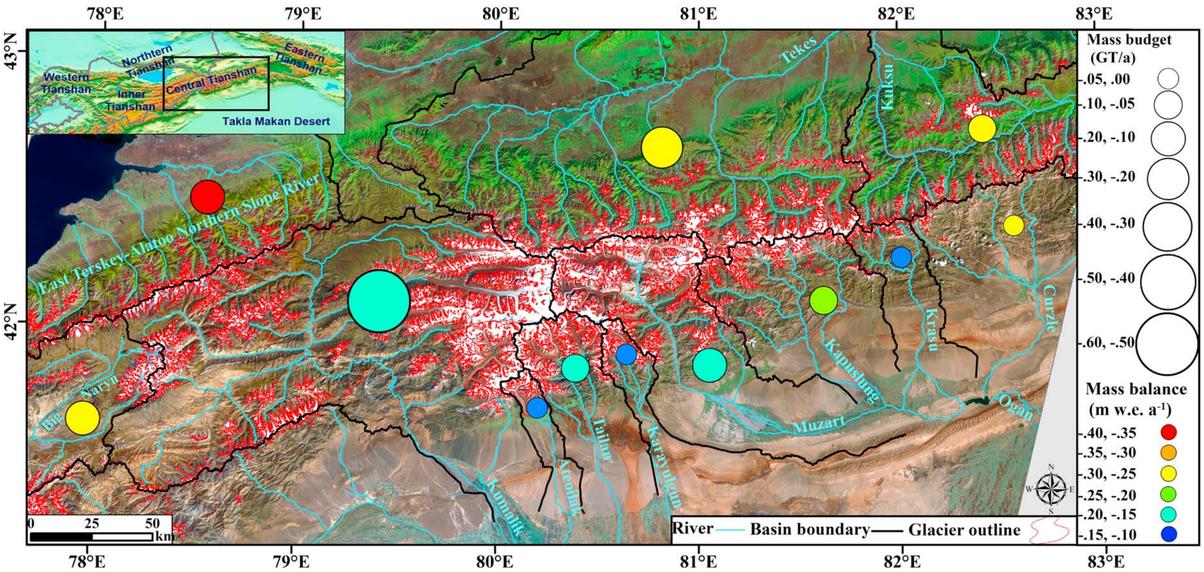

Figure 11. InSAR-based glacier mass changes in 12 river catchments over 2000–2012. The glacier mass balances and budgets in each river catchment are represented by the size and color of a circle, respectively. The densely distributed rivers on the northern slope of East Terskey-Alatoo are considered to belong to one river basin and are named East Terskey-Alatoo Northern Slope Rivers. The background is a mosaic Landsat image (fusion of multispectral band combination 321 (RGB) and panchromatic band 8).

images, SRTM DEM, and Landsat images. As shown in Figure 11 and Table 7, all the river catchments in CTS (the fourth level river basin according to China Glacier Inventory) had a glacier mass loss rate higher than our study area (a density of 900 kg/m^3 was used to transfer the volume change in Li et al., 2017, into mass change). Note that our study area is located in the south of Muzart river catchment, and the glacier mass loss rate of our study area was considerably lower than that of the north part of Muzart river catchment. Previously, Pieczonka and Bolch (2015) derived the region-wide CTS glacier mass balance between ~1975 and 1999 using KH-9 stereo images and the SRTM DEM. Although the quantitative mass balance over our study area has not been calculated separately, we could find that the glacier thickness change patterns presented by Pieczonka and Bolch (2015) were similar to ours, and the relatively strong thinning occurred in the same places. The glacier mass loss rate in the Karayulgun River basin, which is adjacent to our west glacial center (see Figures 1 and 11; a glacierized area of 141.1 km^2, delineated from the Landsat images listed in Table 2), was found to be the lowest (−0.12 ± 0.22 m w.e./a) among the 24 studied basins in the CTS

Table 7
InSAR-Based Geodetic 2000–2012 Glacier Mass Balance of 12 River Catchments in Central Tianshan

Basin name	Glacier area (km^2)	Debris coverage (%)	Coverage of measurements (%)	Mass balance (m/year w.e.)	Mass budget (Gt/year)
Kumalik	2904.6	11.4	84.8	−0.20 ± 0.21	−0.57 ± 0.60
Muzart	1105.2	15.0	62.7	−0.17 ± 0.24	−0.19 ± 0.27
Tekes	1032.5	9.0	93.2	−0.27 ± 0.25	−0.28 ± 0.25
Big Naryn	471[a]	4.0	55.7	−0.25 ± 0.15	−0.12 ± 0.07
Tailan	470.8	17.2	66.6	−0.16 ± 0.21	−0.08 ± 0.10
Kuksu	381.9	5.2	58.1	−0.25 ± 0.24	−0.10 ± 0.09
Kapuslung	314.6	11.1	81.1	−0.21 ± 0.23	−0.07 ± 0.07
ETANSR	266.4	8.1	88.3	−0.39 ± 0.16	−0.10 ± 0.04
Karayulgun	141.1	14.3	85.7	−0.12 ± 0.21	−0.02 ± 0.03
Ateoyilak	100.4	27.2	79.4	−0.12 ± 0.21	−0.01 ± 0.02
Krasu	53.7	7.3	81.2	−0.14 ± 0.24	−0.01 ± 0.01
Curzle	36.8	5.9	12.9	−0.27 ± 0.24	−0.01 ± 0.01

Note. ETANSR = East Terskey-Alatoo Northern Slope Rivers.
[a]The total glacier area of Big Naryn Basin is taken from Hagg et al. (2013).

10.1029/2017JD028150

(Pieczonka & Bolch, 2015). Meanwhile, among the 16 glaciers with individually measured mass balances, the Keqi Keku Zibayi glacier (in the Karayulgun river basin, see Figure 1) is one of the two that gained mass (+0.02 ± 0.22 m w.e./a). The other (Bulantor glacier) locates in the west slope of the Tuomuer-Khan Tengri Mountain Ranges. Moreover, based on geodetic measurement between 1979–1999 and 1999–2009, Pieczonka et al. (2013) pointed out that the glacier mass loss rate in the southwest of the Tuomuer-Khan Tengri Mountain Ranges decelerated in the early 21st century. Therefore, it is objective that the mass balance in our study area between August 1999 and August 2010 is slightly negative.

We tried to find possible reasons for this "anomalous" state from the glacier flow speed map and the climate records. The time series of air temperature and precipitation over the glacierized region in CTS was extracted from the reanalysis gridded climate data set ERA-Interim provided by the European Centre for Medium-Range Weather Forecasts (ECMWF, http://apps.ecmwf.int/datasets/). The ERA-Interim data sets indicate that the summer (May–September) air temperature dropped after entering 21st century. The averaged summer air temperature between 1990 and 2000 was 7.41°C, while between 2000 and 2011, it was lower, being 7.36°C. Although the averaged winter (October–April) air temperature increased (−7.45 versus −7.09°C) and the averaged summer and winter precipitation decreased (586.7 versus 594.2 mm, 194.5 versus 212.9 mm) over the same two periods, the condition became favorable for maintaining glacier mass, because glaciers in CTS are of the summer accumulation type (from 1990 to 2011, the summer precipitation nearly accounted for 75% of the annual precipitation) and temperature usually plays a more effective role than precipitation on adjusting glacier mass. Sheng et al. (2009) reported that a temperature change of 1°C at Kumalik river catchment could lead to 7.2×10^8 m^3 runoff change, while a precipitation change of 100 mm could cause only 0.2×10^8 m^3 of runoff change. Note that the Kumalik river has 58.6% of its runoff coming from glacier meltwater (Sheng et al., 2009). Besides, according to the data collected at Tianshan meteorological station, the long-term annual runoff varies synchronously with the summer temperature (Hagg et al., 2013). Lower summer temperatures not only relieve the glacier mass loss in the glacier ablation zones but also facilitate the mass replenishment in the accumulation zones. However, for the glaciers flowing at a fairly low speed (0.01–0.10 m/day; see Figure 10), the transportation of accumulated mass from the higher reaches needs a long time, and therefore, the mass loss in the lower reaches during the hot years could not be replenished quickly. As a result, the overall mass balance was slightly negative, while glaciers in the east center saw significant thinning in their ablation zones.

In general, the climate change records are consistent with our result; however, they cannot explain why glaciers in our study area are more stable than others in CTS. As shown by the ERA-Interim data sets (Figure 12), our study area does not have a superior cryospheric condition relative to other glacierized regions in CTS. In fact, the multiyear average temperature and precipitation are relatively high and less, respectively (Figure 12). We have discussed the effects of debris cover on glacier mass change. However, the regional glacier debris coverage in our study area is only 9.2%, lower than Kumalik, Tailan, Ateoyilak, and Karayulgun river catchments (see Figure 11 and Table 7). More importantly, the glaciers with relatively high debris coverage in our study area flow much slower than the tree-like large glaciers in the above four regions (Li et al., 2014), which indicates that the debris thickness in our study area is thinner than the above four regions. Therefore, the debris cover is also unlikely to be the major cause of nearly stable glacier state in our study area. Previous studies have reported that glaciers/ice caps in the Inner Tibetan Plateau and East Kunlun Mountain were nearly stable in the early 21st century (Brun et al., 2017; Gardner et al., 2013; Neckel et al., 2014; Yao et al., 2012; Ye et al., 2016, 2017). Such glacier state is not contradictory to the global warming because the climate there is extreme cold and dry and is nearly free of anthropogenic influence. More importantly, glaciers in the Inner Tibetan Plateau and East Kunlun Mountain belong to continental type and are characterized by strong cold storage capability and insensitivity to temperature rise due to the high surface albedo and weak subglacial ablation. As mentioned above, most glaciers in our study area flow at fairly low speeds, except the ones with thickening in the ablation zones, which show some features of surge (to be conservative, we only marked out three surge-type glaciers in Figures 7 and 8). Unlike the large glaciers in the Himalayas (Gardelle et al., 2013; Kääb et al., 2012) and other parts of CTS (Li et al., 2017), the relatively small ones in our study area may have considerable lower englacial temperature and therefore slight subglacial ablation and weak basal sliding. Glaciers in the east center have clean surfaces that ensure high albedo, while glaciers in the west center have debris cover that partly insulates the external heat. Furthermore, the major part of the exposed glacier ablation zone in our study area is distributed at an altitude over 3,800 m a.s.l.,

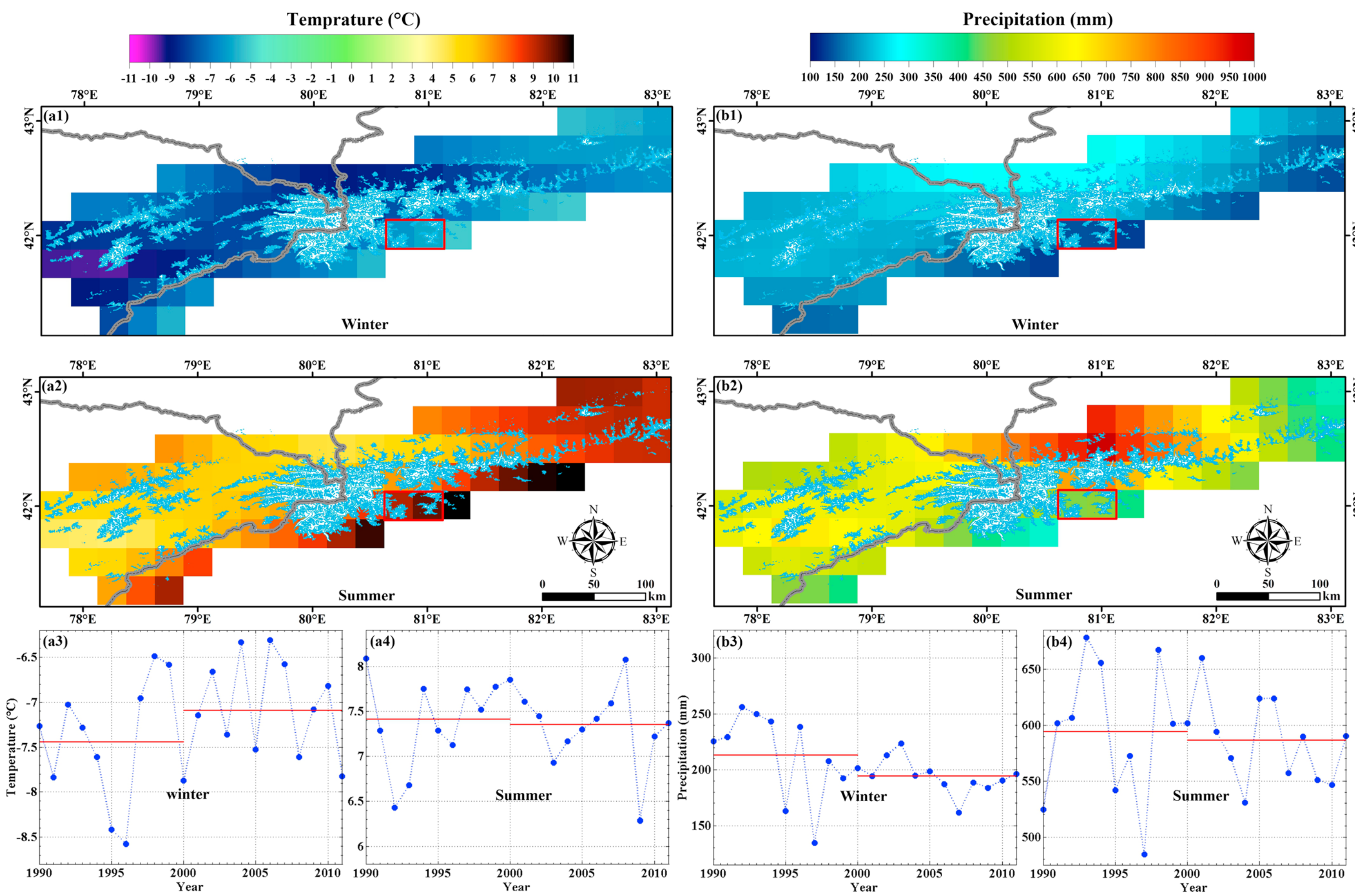

Figure 12. Air temperature and precipitation variations in Central Tianshan glacierized region over 1990–2011. The data are extracted from 0.25° reanalysis grid climate data set provided by ECMWF (http://apps.ecmwf.int/datasets/). (a1, a2) Spatial distribution of 1990–2011 mean summer (May–September) and winter (October–April) temperatures, respectively; (a3, a4) temporal variations of mean summer and winter temperatures, respectively; (b1, b2) spatial distribution of 1990–2011 mean summer and winter cumulative precipitations, respectively; (b3, b4) temporal variations of regional mean summer and winter cumulative precipitations, respectively. The red lines in (a3, a4) and (b3, b4) are the averages of the data of different periods. The red rectangles in (a1), (a2), (b1), and (b2) mark our study area.

which is higher than most glacial areas in CTS. Therefore, for the studied glaciers, the stronger cold storage capability ensured by lower englacial temperature and higher altitude may be the main reasons for a more stable state.

5. Conclusion

In this study, we conducted glacier mass balance measurements in the catchments of Muzart and Karayulgun rivers (CTS) based on a geodetic method and the ALOS/PRISM images and SRTM DEM. The ICESat/GLAS GLA14 land elevation product and Landsat-7/ETM+ L1T images were employed as height and horizontal control sources in the generation of ALOS/PRISM DEM. After coregistration, the two DEMs were differenced, and the systematic height difference bias related to planimetric position, terrain aspect, and curvature was corrected based on the assumption that the bias of the glacial and nonglacial height differences is common. Furthermore, C-band penetration was measured from the differences between the simultaneously acquired C-band and X-band SRTM DEMs. Terrain mapping faces a challenge in this area since no open flat zones can be found. However, our approach still obtained reasonable glacial height changes. Generally, the exposed glacier tongues and those covered by debris were found to experience significant and moderate thinning, respectively. The main ridges crossing the way of prevailing current are with quite different glacier sizes, mass balance, flow speed, and surge activities on its two sides. Glaciers with a higher flow speed and a greater chance of receiving precipitation were found to experience slight thickening in their tongues. For two glacial centers in our study area, the newly derived 2000–2011 mass balances were -0.03 ± 0.17 and -0.06 ± 0.17 m w.e./a, respectively, much lower than that of other glacierized zones in the CTS. In order to confirm this "anomalous" result, we performed another geodetic measurement (2000–2012) based on TanDEM-X images and SRTM DEM. The results were very close to that by ALOS/PRISM (0.01 ± 0.17 and −0.04 ± 0.17 m w.e./a for two centers, respectively). The strong capability of cold storage and the temperature drop in the early 21st century may account for the nearly stable glacier state. For the downstream settlements controlled by arid climate, the reveal of stable glacier state in the catchments of Karayulgun and Muzart rivers shall be positive news. However, further investigations are still required to validate the glacier state and to confirm the reasons why the glaciers change slightly.

Acknowledgments
This work was supported by the Strategic Priority Research Program of Chinese Academy of Sciences (XDA20100101), the National Key Research and Development Program of China (2018YFA0605504), and the scientific research start-up programs of Central South University (grants 202044003, 506030101, and 502045001), and the general programs from the Research Grants Council of the Hong Kong Special Administrative Region (PolyU 5146/11E), the National Natural Science Foundation of China (41474007, 41701500, and 41574005), and the Postdoctoral Science Foundation of China (2018 M630908). The ALOS/PRISM images, the TanDEM-X/CoSSC images, the Landsat L1T images, the ICESat/GLAS GLA14 product, the SRTM DEM, the China Glacier Inventory (revised version 1), and the ERA-Interim data set were provided by JAXA (P1246002), the DLR (jiali_XTI_GLAC6371 and jiali_XTI_GLAC6767), the USGS, the NSIDC DAAC, http://www.cgiar-csi.org/data, http://westdc.westgis.ac.cn/glacier, and ECMWF, respectively.

References

Atwood, D. K., Guritz, R. M., Muskett, R. R., Lingle, C. S., Sauber, J. M., & Freymueller, J. T. (2007). DEM control in Arctic Alaska with ICESat laser altimetry. *IEEE Transactions on Geoscience and Remote Sensing*, *45*(11), 3710–3720. https://doi.org/10.1109/TGRS.2007.904335

Bamber, J. L., & Rivera, A. (2007). A review of remote sensing methods for glacier mass balance determination. *Global and Planetary Change*, *59*(1-4), 138–148. https://doi.org/10.1016/j.gloplacha.2006.11.031

Berthier, E., Arnaud, Y., Vincent, C., & Rémy, F. (2006). Biases of SRTM in high-mountain areas. Implications for the monitoring of glacier volume changes. *Geophysical Research Letters*, *33*, L08502. https://doi.org/10.1029/2006GL025862

Berthier, E., Cabot, V., Vincent, C., & Six, D. (2016). Decadal region-wide and glacier-wide mass balances derived from multi-temporal ASTER satellite digital elevation models. Validation over the Mont-Blanc area. *Frontiers in Earth Science*, *4*. https://doi.org/10.3389/feart.2016.00063

Berthier, E., Schiefer, E., Clarke, G. K. C., Menounos, B., & Rémy, F. (2010). Contribution of Alaskan glaciers to sea-level rise derived from satellite imagery. *Nature Geoscience*, *3*(2), 92–95. https://doi.org/10.1038/ngeo737

Berthier, E., & Toutin, T. (2008). SPOT5-HRS digital elevation models and the monitoring of glacier elevation changes in North-West Canada and South-East Alaska. *Remote Sensing of Environment*, *112*(5), 2443–2454. https://doi.org/10.1016/j.rse.2007.11.004

Bhambri, R., Hewitt, K., Kawishwar, P., & Pratap, B. (2017). Surge-type and surge-modified glaciers in the Karakoram. *Scientific Reports*, *7*(1), 15391. https://doi.org/10.1038/s41598-017-15473-8

Bolch, T., Pieczonka, T., & Benn, D. I. (2011). Multi-decadal mass loss of glaciers in the Everest area (Nepal, Himalaya). *The Cryosphere*, *5*(2), 349–358. https://doi.org/10.5194/tc-5-349-2011

Brun, F., Berthier, E., Wagnon, P., Kääb, A., & Treichler, D. (2017). A spatially resolved estimate of High Mountain Asia glacier mass balances from 2000 to 2016. *Nature Geoscience*, *10*(9), 668–673. https://doi.org/10.1038/ngeo2999

Cox, L. H., & March, R. S. (2004). Comparison of geodetic and glaciological mass-balance techniques, Gulkana Glacier, Alaska, U.S.A. *Journal of Glaciology*, *50*(170), 363–370. https://doi.org/10.3189/172756504781829855

Duan, J. J., Cao, X. L., Shen, Y. P., Gao, Q. Z., & Wang, S. D. (2010). Surface water resources and its trends in Weigan River basin on the south slope of Tianshan, China during 1956–2007. *Journal of Glaciology and Geocryology*, *32*(6), 1211–1219. (in Chinese with English abstract)

Farinotti, D., Longuevergne, L., Moholdt, G., Duethmann, D., Mölg, T., Bolch, T., et al. (2015). Substantial glacier mass loss in the Tianshan over the past 50 years. *Nature Geoscience*, *8*(9), 716–722. https://doi.org/10.1038/ngeo2513

Fujita, K., Takeuchi, N., Nikitin, S. A., & Surazakov, A. B. (2011). Favorable climatic regime for maintaining the present-day geometry of the Gregoriev Glacier, Inner Tianshan. *The Cryosphere*, *5*(3), 539–549. https://doi.org/10.5194/tc-5-539-2011

Gardelle, J., Berthier, E., & Arnaud, Y. (2012a). Slight mass gain of Karakoram glaciers in the early 21st century. *Nature Geoscience*, *5*(5), 322–325. https://doi.org/10.1038/ngeo1450

Gardelle, J., Berthier, E., & Arnaud, Y. (2012b). Impact of resolution and radar penetration on glacier elevation changes computed from DEM differencing. *Journal of Glaciology*, *58*(208), 419–422. https://doi.org/10.3189/2012JoG11J175

Gardelle, J., Berthier, E., Arnaud, Y., & Kääb, A. (2013). Region-wide glacier mass balances over the Pamir-Karakoram-Himalaya during 1999–2011. *The Cryosphere*, *7*(4), 1263–1286. https://doi.org/10.5194/tc-7-1263-2013

Gardner, A. S., Moholdt, G., Cogley, J. G., Wouters, B., Arendt, A. A., Wahr, J., et al. (2013). A reconciled estimate of glacier contributions to sea level rise: 2003 to 2009. *Science*, *340*(6134), 852–857. https://doi.org/10.1126/science.1234532

Guo, W. Q., Liu, S., Xu, J., Wu, L., Shangguan, D., Yao, X., et al. (2015). The second Chinese glacier inventory: Data, methods and results. *Journal of Glaciology*, *61*(226), 357–372. https://doi.org/10.3189/2015JoG14J209

Hagg, W., Mayer, C., Lambrecht, A., & Helm, A. (2008). Sub-debris melt rates on Southern Inylchek Glacier, Central Tian Shan. *Geografiska Annaler Series A Physical Geography*, *90*(1), 55–63. https://doi.org/10.1111/j.1468-0459.2008.00333.x

Hagg, W., Mayer, C., Lambrecht, A., Kriegel, D., & Aziov, E. (2013). Glacier changes in the Big Naryn basin, Central Tian Shan. *Global and Planetary Change*, *110* (Part A), 40–50.

Hajnsek, I., Busche, T., Fiedler, H., Krieger, G., Buckreuss, S., Zink, M., et al. (2010). *TanDEM-X science plan, version 1, TD-PD-PL-0069, TanDEM-X ground segment*. Oberpfaffenhofen, Germany: Microwave and Radar Institute, DLR.

Höhle, J., & Höhle, M. (2009). Accuracy assessment of digital elevation models by means of robust statistical methods. *ISPRS Journal of Photogrammetry and Remote Sensing*, *64*(4), 398–406. https://doi.org/10.1016/j.isprsjprs.2009.02.003

Holzer, N., Vijay, S., Yao, T., Xu, B., Buchroithner, M., & Bolch, T. (2015). Four decades of glacier variations at Muztagh Ata (eastern Pamir): A multi-sensor study including Hexagon KH-9 and Pléiades data. *The Cryosphere*, *9*(6), 2071–2088. https://doi.org/10.5194/tc-9-2071-2015

Kääb, A. (2005). *Remote sensing of mountain glaciers and permafrost creep*. Zürich: Geographisches Institut der Universität Zürich.

Kääb, A. (2008). Glacier volume changes using ASTER satellite stereo and ICESat GLAS laser altimetry. A test study on Edgeyøa, eastern Svalbard. *IEEE Transactions on Geoscience and Remote Sensing*, *46*(10), 2823–2830. https://doi.org/10.1109/TGRS.2008.2000627

Kääb, A., Berthier, E., Nuth, C., Gardelle, J., & Arnaud, Y. (2012). Contrasting patterns of early twenty-first-century glacier mass change in the Himalayas. *Nature*, *488*(7412), 495–498. https://doi.org/10.1038/nature11324

Koblet, T., Gärtner-Roer, I., Zemp, M., Jansson, P., Thee, P., Haeberli, W., & Holmlund, P. (2010). Reanalysis of multi-temporal aerial images of Storglaciären, Sweden (1959–99) – Part 1: Determination of length, area, and volume changes. *The Cryosphere*, *4*(3), 333–343. https://doi.org/10.5194/tc-4-333-2010

Kronenberg, M., Barandun, M., Hoelzle, M., Huss, M., Farinotti, D., Azisov, E., et al. (2016). Mass-balance reconstruction for Glacier No. 354, Tianshan, from 2003 to 2014. *Annals of Glaciology*, *57*(71), 92–102. https://doi.org/10.3189/2016AoG71A032

Lamsal, D., Sawagaki, T., & Watanabe, T. (2011). Digital terrain modelling using Corona and ALOS PRISM data to investigate the distal part of Imja glacier, Khumbu Himal, Nepal. *Journal of Mountain Science*, *8*(3), 390–402. https://doi.org/10.1007/s11629-011-2064-0
Li, J., Li, Z. W., Ding, X. L., Wang, Q. J., Zhu, J. J., & Wang, C. C. (2014). Investigating mountain glacier motion with the method of SAR intensity-tracking: Removal of topographic effects and analysis of the dynamic patterns. *Earth-Science Reviews*, *138*, 179–195. https://doi.org/10.1016/j.earscirev.2014.08.016
Li, J., Li, Z. W., Zhu, J. J., Li, X., Xu, B., Wang, Q. J., et al. (2017). Early 21st century glacier thickness changes in the Central Tien Shan. *Remote Sensing of Environment*, *192*, 12–29. https://doi.org/10.1016/j.rse.2017.02.003
Li, X., Cheng, G., Jin, H., Kang, E., Che, T., Jin, R., et al. (2008). Cryospheric change in China. *Global and Planetary Change*, *62*(3–4), 210–218. https://doi.org/10.1016/j.gloplacha.2008.02.001
Lønne, I. (2016). A new concept for glacial geological investigations of surges, based on High-Arctic examples (Svalbard). *Quaternary Science Reviews*, *132*, 74–100. https://doi.org/10.1016/j.quascirev.2015.11.009
Luckman, A., Quincey, D., & Bevan, S. (2007). The potential of satellite radar interferomery and feature tracking for monitoring flow rates of Himalayan glaciers. *Remote Sensing of Environment*, *111*(2–3), 172–181. https://doi.org/10.1016/j.rse.2007.05.019
Muskett, R. R., Lingle, C. S., Sauber, J. M., Rabus, B. T., & Tangborn, W. V. (2008). Acceleration of surface lowering on the tidewater glaciers of Icy Bay, Alaska, U.S.A. from InSAR DEMs and ICESat altimetry. *Earth and Planetary Science Letters*, *265*(3-4), 345–359. https://doi.org/10.1016/j.epsl.2007.10.012
Neckel, N., Kropáček, J., Bolch, T., & Hochschild, V. (2014). Glacier mass changes on the Tibetan Plateau 2003–2009 derived from ICESat laser altimetry measurements. *Environmental Research Letters*, *9*(9), 468–475.
Nuimura, T., Sakai, A., Taniguchi, K., Nagai, H., Lamsal, D., Tsutaki, S., et al. (2015). The GAMDAM Glacier Inventory: A quality controlled inventory of Asian glaciers. *The Cryosphere*, *9*(3), 849–864. https://doi.org/10.5194/tc-9-849-2015
Nuth, C., & Kääb, A. (2011). Co-registration and bias corrections of satellite elevation data sets for quantifying glacier thickness change. *The Cryosphere*, *5*(1), 271–290. https://doi.org/10.5194/tc-5-271-2011
Paul, F. (2008). Calculation of glacier elevation changes with SRTM: Is there an elevation-dependent bias? *Journal of Glaciology*, *54*(188), 945–946. https://doi.org/10.3189/002214308787779960
Paul, F., Bolch, T., Kääb, A., Nagler, T., Nuth, C., Scharrer, K., et al. (2015). The glaciers climate change initiative: Methods for creating glacier area, elevation change and velocity products. *Remote Sensing of Environment*, *162*, 408–426. https://doi.org/10.1016/j.rse.2013.07.043
Paul, F., Huggel, C., & Kääb, A. (2004). Combining satellite multispectral image data and a digital elevation model for mapping debris-covered glaciers. *Remote Sensing of Environment*, *89*(4), 510–518. https://doi.org/10.1016/j.rse.2003.11.007
Peduzzi, P., Herold, C., & Silverio, W. (2010). Assessing high altitude glacier thickness, volume and area changes using field, GIS and remote sensing techniques the case of Nevado Coropuna. *The Cryosphere*, *4*(3), 313–323. https://doi.org/10.5194/tc-4-313-2010
Petrakov, D., Shpuntova, A., Aleinikov, A., Kääb, A., Kutuzov, S., Lavrentiev, I., et al. (2016). Accelerated glacier shrinkage in the Ak-Shyirak massif, Inner Tianshan, during 2003–2013. *Science of the Total Environment*, *562*, 364–378. https://doi.org/10.1016/j.scitotenv.2016.03.162
Pieczonka, P., Bolch, T., Wei, J. F., & Liu, S. Y. (2013). Heterogeneous mass loss of glaciers in the Aksu-Tarim Catchment (Central Tien Shan) revealed by 1976 KH-9 Hexagon and 2009 SPOT-5 stereo imagery. *Remote Sensing of Environment*, *130*, 233–244. https://doi.org/10.1016/j.rse.2012.11.020
Pieczonka, T., & Bolch, T. (2015). Region-wide glacier mass budgets and area changes for the Central Tien Shan between ~1975 and 1999 using Hexagon KH-9 imagery. *Global and Planetary Change*, *128*, 1–13. https://doi.org/10.1016/j.gloplacha.2014.11.014
Pieczonka, T., Bolch, T., & Buchroithner, M. F. (2011). Generation and evaluation of multi-temporal digital terrain models of the Mt. Everest area from different optical sensors. *ISPRS Journal of Photogrammetry and Remote Sensing*, *66*(6), 927–940. https://doi.org/10.1016/j.isprsjprs.2011.07.003
Rabus, B., Eineder, M., Roth, A., & Bamler, R. (2003). The Shuttle Radar Topography Mission—A new class of digital elevation models acquired by spaceborne radar. *ISPRS Journal of Photogrammetry and Remote Sensing*, *57*(4), 241–262. https://doi.org/10.1016/S0924-2716(02)00124-7
Racoviteanu, A. E., Manley, W. F., Arnaud, Y., & Williams, M. W. (2007). Evaluating digital elevation models for glaciologic applications: An example from Nevado Coropuna, Peruvian Andes. *Global and Planetary Change*, *59*(1-4), 110–125. https://doi.org/10.1016/j.gloplacha.2006.11.036
Racoviteanu, A. E., Paul, F., Raup, B., Khalsa, S. J. S., & Armstrong, R. (2009). Challenges and recommendations in mapping of glacier parameters from space: Results of the 2008 Global Land Ice Measurements from space (GLIMS) workshop, Boulder, Colorado, USA. *Annals of Glaciology*, *50*(53), 53–69. https://doi.org/10.3189/172756410790595804
Ren, B. H. (1990). *Chinese glaciers*. Lanzhou: Gansu Education Press. (in Chinese)
Rignot, E., Echelmeyer, K., & Krabill, W. (2001). Penetration depth of interferometric synthetic-aperture radar signals in snow and ice. *Geophysical Research Letters*, *28*, 3501–3504. https://doi.org/10.1029/2000GL012484
Rodríguez, E., Morris, C. S., & Belz, J. E. (2006). A global assessment of the SRTM performance. *Photogrammetric Engineering & Remote Sensing*, *72*(3), 249–260. https://doi.org/10.14358/PERS.72.3.249
Sansosti, E., Berardino, P., Manunta, M., Serafino, F., & Fornaro, G. (2006). Geometrical SAR image registration. *IEEE Transactions on Geoscience and Remote Sensing*, *44*(10), 2861–2870. https://doi.org/10.1109/TGRS.2006.875787
Scherler, D., Bookhagen, B., & Strecker, M. R. (2011). Spatially variable response of Himalayan glaciers to climate change affected by debris cover. *Nature Geoscience*, *4*(3), 156–159. https://doi.org/10.1038/ngeo1068
Schiefer, E., Menounos, B., & Wheate, R. (2007). Recent volume loss of British Columbian glaciers, Canada. *Geophysical Research Letters*, *34*, L16503. https://doi.org/10.1029/2007GL030780
Schutz, B. E., Zwally, H. J., Shuman, C. A., Hancock, D., & DiMarzio, J. P. (2005). Overview of the ICESat mission. *Geophysical Research Letters*, *32*, L21S01. https://doi.org/10.1029/2005GL024009
Shangguan, D. H., Bolch, T., Ding, Y. J., Kröhnert, M., Pieczonka, T., Wetzel, H. U., & Liu, S. Y. (2015). Mass changes of Southern and Northern Inylchek Glacier, Central Tian Shan, Kyrgyzstan, during ~1975 and 2007 derived from remote sensing data. *The Cryosphere*, *9*(2), 703–717. https://doi.org/10.5194/tc-9-703-2015
Sheng, Y. P., Wang, G. Y., Ding, Y. J., Mao, W. Y., Liu, S. Y., Wang, S. D., & Mamatkanov, D. M. (2009). Changes in glacier mass balance in watershed of Sary Jaz-Kumarik rivers of Tianshan Mountains in 1957–2006 and their impact on water resources and trend to end of the 21th century (in Chinese with English abstract). *Chinese Journal of Glaciology and Geocryology*, *31*(5), 792–800.
Shi, Y. F., Huang, M. H., Yao, T. D., & He, Y. Q. (2008). *Glaciers and related environments in China*. Beijing: Science Press.
Sorg, A., Bolch, T., Stoffel, M., Solomina, O., & Beniston, M. (2012). Climate change impacts on glaciers and runoff in Tianshan (Central Asia). *Nature Climate Change*, *2*(10), 725–731. https://doi.org/10.1038/NCLIMATE1592

Journal of Geophysical Research: Atmospheres 10.1029/2017JD028150

Strozzi, T., Luckman, A., Murray, T., Wegmülller, U., & Werner, C. L. (2002). Glacier motion estimation using SAR offset-tracking procedures. *IEEE Transactions on Geoscience and Remote Sensing*, *40*(11), 2384–2391. https://doi.org/10.1109/TGRS.2002.805079

Su, Z., Song, G. P., & Wang, L. L. (1985). *Glacial and meteorology in mountain Tuomuer district, Tianshan*. Urumqi: Xinjiang People's Publish House. (in Chinese)

Surazakov, A. B., & Aizen, V. B. (2006). Estimating volume change of mountain glaciers using SRTM and map-based topographic data. *IEEE Transactions on Geoscience and Remote Sensing*, *44*(10), 2991–2995. https://doi.org/10.1109/TGRS.2006.875357

Tennant, C., Menounos, B., Ainslie, B., Shea, J., & Jackson, P. (2012). Comparison of modeled and geodetically-derived glacier mass balance for Tiedemann and Klinaklini glaciers, southern Coast Mountains, British Columbia, Canada. *Global and Planetary Change*, *82-83*, 74–85. https://doi.org/10.1016/j.gloplacha.2011.11.004

Vincent, C., Ramanathan, A., Wagnon, P., Dobhal, D. P., Linda, A., Berthier, E., et al. (2013). Balanced conditions or slight mass gain of glaciers in the Lahaul and Spiti region (northern India, Himalaya) during the nineties preceded recent mass loss. *The Cryosphere*, *7*(2), 569–582. https://doi.org/10.5194/tc-7-569-2013

WGMS (2015). *Global glacier change bulletin no. 1 (2012–2013)*. Zurich, Switzerland: ICSU (WDS)/IUGG (IACS)/UNEP/UNESCO/WMO, World Glacier Monitoring Service. https://doi.org/10.5904/wgms-fog-2015-11

Willis, M. J., Melkonian, A. K., Pritchard, M. E., & Ramage, J. M. (2012). Ice loss rates at the northern Patagonian icefield derived using a decade of satellite remote sensing. *Remote Sensing of Environment*, *117*, 184–198. https://doi.org/10.1016/j.rse.2011.09.017

Xie, C. W., Ding, Y. J., Chen, C. P., & Han, T. D. (2007). Study on the change of Keqikaer glacier during the last 30 years, Mt. Tuomuer, western China. *Environmental Geology*, *51*, 1651–1170.

Xie, Z. C., & Liu, C. H. (2010). *Introduction of glaciology*. Beijing: Science Press. (in Chinese)

Yao, T. D., Thompson, L., Yang, W., Yu, W., Gao, Y., Guo, X., et al. (2012). Different glacier status with atmospheric circulations in Tibetan Plateau and surroundings. *Nature Climate Change*, *2*(9), 663–667. https://doi.org/10.1038/nclimate1580

Ye, Q. H., Bolch, T., Naruse, R., Wang, Y., Zong, J., Wang, Z., et al. (2015). Glacier mass changes in Rongbuk catchment on Mt. Qomolangma from 1974 to 2006 based on topographic maps and ALOS PRISM data. *Journal of Hydrology*, *530*, 273–280. https://doi.org/10.1016/j.jhydrol.2015.09.014

Ye, Q. H., Cheng, W. M., Zhao, Y. L., Zong, J. B., & Zhao, R. (2016). A review on the research of glacier changes on the Tibetan Plateau by remote sensing technologies. *Journal of Geo-information Science*, *18*(7), 920–930. https://doi.org/10.3724/SP.J.1047.2016.00920 (In Chinese with English abstract)

Ye, Q. H., Zong, J. B., Tian, D. L., Cogley, J. G., Song, C. Q., & Guo, W. Q. (2017). Glacier changes on the Tibetan Plateau derived from Landsat imagery: Mid-1970s–2000–13. *Journal of Glaciology*, *63*(238), 273–287. https://doi.org/10.1017/jog.2016.137

Zhang, Y., Liu, S. Y., Ding, Y. J., Li, J., & Shangguan, D. H. (2006). Preliminary study of mass balance on the Keqicar Baxi glacier on the south slopes of Tianshan Mountains. *Journal of Glaciology and Geocryology*, *28*(4), 477–484. (in Chinese with English abstract)

Zhou, Y. S., Li, Z. W., & Li, J. (2017). Slight glacier mass loss in the Karakoram region during the 1970s to 2000 revealed by KH-9 images and SRTM DEM. *Journal of Glaciology*, *63*(238), 331–342. https://doi.org/10.1017/jog.2016.142